

On the projected changes in New Zealand's wave climate and its main drivers

Albuquerque, João; Antolínez, Jose A.A.; Méndez, Fernando J.; Coco, Giovanni

DOI

[10.1080/00288330.2022.2135116](https://doi.org/10.1080/00288330.2022.2135116)

Publication date

2022

Document Version

Final published version

Published in

New Zealand Journal of Marine and Freshwater Research

Citation (APA)

Albuquerque, J., Antolínez, J. A. A., Méndez, F. J., & Coco, G. (2022). On the projected changes in New Zealand's wave climate and its main drivers. *New Zealand Journal of Marine and Freshwater Research*, 58(1), 89-126. <https://doi.org/10.1080/00288330.2022.2135116>

Important note

To cite this publication, please use the final published version (if applicable).
Please check the document version above.

Copyright

Other than for strictly personal use, it is not permitted to download, forward or distribute the text or part of it, without the consent of the author(s) and/or copyright holder(s), unless the work is under an open content license such as Creative Commons.

Takedown policy

Please contact us and provide details if you believe this document breaches copyrights.
We will remove access to the work immediately and investigate your claim.

Green Open Access added to TU Delft Institutional Repository

'You share, we take care!' - Taverne project

<https://www.openaccess.nl/en/you-share-we-take-care>

Otherwise as indicated in the copyright section: the publisher is the copyright holder of this work and the author uses the Dutch legislation to make this work public.



ISSN: 1177-3130

On the projected changes in New Zealand's wave climate and its main drivers

João Albuquerque, Jose A. A. Antolínez, Fernando J. Méndez & Giovanni Coco

To cite this article: João Albuquerque, Jose A. A. Antolínez, Fernando J. Méndez & Giovanni Coco (2022): On the projected changes in New Zealand's wave climate and its main drivers, New Zealand Journal of Marine and Freshwater Research, DOI: [10.1080/00288330.2022.2135116](https://doi.org/10.1080/00288330.2022.2135116)

To link to this article: <https://doi.org/10.1080/00288330.2022.2135116>

 View supplementary material [↗](#)

 Published online: 03 Nov 2022.

 Submit your article to this journal [↗](#)

 Article views: 105

 View related articles [↗](#)

 View Crossmark data [↗](#)

RESEARCH ARTICLE



On the projected changes in New Zealand's wave climate and its main drivers

João Albuquerque ^a, Jose A. A. Antolínez ^b, Fernando J. Méndez ^c and Giovanni Coco ^a

^aSchool of Environment, University of Auckland, Auckland, New Zealand; ^bDepartment of Hydraulic Engineering, Faculty of Civil Engineering and Geosciences, Delft University of Technology, Delft, Netherlands; ^cDepartamento de Ciencias y Técnicas del Agua y del Medio Ambiente, E.T.S.I de Caminos, Canales y Puertos, Universidad de Cantabria, Santander, Spain

ABSTRACT

Wave climatologies from historical and projected simulations of the ACCESS1.0, MIROC5 and CNRM-CM5 Global Circulation Models (GCM) were sourced from the Coordinated Ocean Wave Climate Project (COWCLIP) and downscaled using the SWAN wave model. Biases between GCM's historical simulations and a regional hindcast were assessed, and the two best-performing models (ACCESS1.0, MIROC5) had their projections analysed. A general increase in wave height and period was observed along the south/west, together with a decrease in H_s along the north/east coasts. The projected near-term (NEA21C) period shows mostly a H_s increase, whilst for the long-term (END21C) period, increased and decreased H_s are present. The areas of statistically significant changes are larger in the END21C than in the NEA21C period. The wave direction change is counter-clockwise along the west and clockwise along the east coasts. This study is a first assessment of historical and projected GCM-forced waves along New Zealand and the database we generated can be of great value for renewable energy research, risk assessment and the mitigation of future coastal hazards.

ARTICLE HISTORY

Received 7 October 2020
Accepted 4 October 2022

HANDLING EDITOR

Craig Stevens

KEYWORDS

CMIP5; global climate projections; New Zealand; wind waves; multimodal spectra; wave downscaling; SWAN

1. Introduction

The interest in the effects of climate change over the present wind-waves has increased in recent years. Anticipating the potential alterations of wind wave characteristics has become crucial to define strategies of mitigation and adaptation for future coastal hazards, in order to minimise their impact on the economy, society and environment.

New Zealand's shorelines are exposed to a variety of high-energy wave climates, such as the Tasman Sea, and the Pacific, Southern and Indian Oceans. Waves interact with both natural and artificial coastal features and are the main drivers of beach morphodynamics processes such as erosion or accretion. The intensity of such processes is modulated by the seasonal changes in meteorological conditions, which can be intensified or diminished by atmospheric anomalies (Masselink and Pattiaratchi 2001; Ashok et al. 2007; Kidston et al. 2009; Griffiths 2011).

CONTACT João Albuquerque  j.dealbuquerque@auckland.ac.nz

 Supplemental data for this article can be accessed online at <https://doi.org/10.1080/00288330.2022.2135116>.

© 2022 The Royal Society of New Zealand

A number of studies assisted in the understanding of how atmospheric anomalies influence the wind wave climate at the global and regional scales and how often they occur (Cox and Swail 2001; Ashok et al. 2007; Stopa et al. 2013; Marshall et al. 2018). In New Zealand, the wave systems present along the west coast are a combination of wind-sea waves generated by the predominant westerlies and swells generated in the Indian and Southern oceans, the latter also reaching the south and southeast coasts. The northeast coast is mostly exposed to wave systems generated by northeasterly winds, but also shows developing southwesterly wave systems off this coast due to westerly winds (Gorman et al. 2003b; Rueda et al. 2019; Albuquerque et al. 2021). Studies have found a number of atmospheric indices (i.e. an index that describes the state and changes of the climate system) associated with the wave climate around New Zealand. For example, large positive anomalies (> 7) of the Southern Oscillation Index (SOI) (Chen 1982) characterise La Niña events, which increase the occurrence of northeasterly winds, and consequently waves along the east coasts of the North Island. The negative/El Niño phase of the SOI has the opposite effect, increasing the southwesterly winds and waves that reach the south and west coasts of New Zealand (Gordon 1986). The Southern Annular Mode (SAM) causes an easterly wind anomaly on the austral summer, anomalous northeasterly (northwesterly) winds along the North (South) Island during the austral winter (Kidston et al. 2009), and an increased frequency of tropical cyclones undergoing extra-tropical transition near New Zealand during its positive phase (Diamond and Renwick 2015). The Dipole Mode Index (DMI), also known as Indian Dipole Mode weakens (enhances) the storm-track over the northern (southern) New Zealand during the austral winter on its positive phase while the opposite occurs during its negative phases (Ashok et al. 2007; Griffiths 2011). A wave height increase is observed throughout the west and southern coasts of New Zealand during negative phases of the Zonal Wave-number-3 Pattern (ZW3) due to the associated zonal flow (Godoi et al. 2016). Finally, as described in Rueda et al. (2019), the Madden-Julien Oscillation (MJO) (Madden and Julian 1971), influences regional circulation and climate in the New Zealand region. Such influence is associated with smaller waves throughout the country during phases 6 and 7, and an increase in the wave height along either the northeast or the southeast coasts during phases 2 and 3.

Regardless of the contribution of all the aforementioned studies, how the long-term changes in global temperature are likely to affect the atmospheric circulation in the twenty-first century, and consequently the waves throughout New Zealand, remains uncertain. The refinement of global circulation models (GCMs) during the fifth phase of the Climate Model Intercomparison Project (CMIP5) (Taylor et al. 2012) allowed for assessments of the future variability of atmospheric parameters such as storm patterns, temperature and precipitation under different representative concentration pathways (RCP) scenarios (Favre and Gershunov 2009; Moss et al. 2010; Sillmann et al. 2013; Feng et al. 2014). However, the ocean component of such models does not account for wave generation processes, as well as the feedback of such processes into the atmosphere (Cavaleri et al. 2012; Couvelard et al. 2020). As the wind forcings of GCMs were employed to generate global (Mori et al. 2010; Hemer et al. 2013) and local wave climate projections (Lionello et al. 2008), a coordinated effort to design a framework to conduct these simulations, as well as comprehensively assess models' results and uncertainties was established by the Coordinated Ocean Wave Climate Project

(COWCLIP) (Hemer et al. 2012) project. As a result, many of the following dynamical and statistical wave climate projections studies (Erikson et al. 2015; Wang et al. 2015; Hemer and Trenham 2016; Mentaschi et al. 2017; Timmermans et al. 2017; Camus et al. 2017; Semedo et al. 2018; Brichenno and Wolf 2018) contributed to a comprehensive assessment of robustness and uncertainties of wind wave projections (Morim et al. 2019).

The projected changes along the Southern Ocean are driven by a southward shift and intensification of the westerly jet as well as a poleward shift of the high-pressure sub-tropical ridge (Hemer et al. 2013; Collins et al. 2013) (sub-tropical high hereinafter), which restricts the extra-tropical storm tracks to higher latitudes. However, these shifts are modulated by factors such as the GCMs' present bias of the westerly jet location (Barnes and Polvani 2013), ozone recovery (Arblaster et al. 2011), as well as the coherence of eddy feedbacks (Simpson et al. 2012) and upper-level meridional temperature gradient changes (Rivière 2011).

Among the converging findings, an increase in the storm activity along the higher latitudes of this area was observed by Taylor et al. (2012) in an analysis of the projected climate for the end of the century. Dobrynin et al. (2012) have also identified an increase in wind speeds and wave heights towards the end of the century while analysing global CMIP5 projections from an earth-system model under RCP4.5 and RCP8.5. Similar findings were also observed by Wang et al. (2014) along latitudes south of 45°S towards the year 2100 in an analysis of a statistical ensemble of 20 CMIP5 models for the RCP8.5 scenario. The agreement between these studies was quantified by Hemer et al. (2013) as an increase in wave height of approximately 7.1% (8.1% during winter) along the Southern Ocean area. The increase in the extreme events along the same area was found to range between 5% and 15% by Meucci et al. (2020).

It should be noted that, despite the GCMs ability to reproduce tropical cyclones, the resolution of the projections ($\sim 1.5^\circ$) is relatively coarse to accurately simulate the intensity and size of such storms (Camargo and Wing 2016). Likewise, despite the wave field resolution of these studies ($\sim 1^\circ$) be sufficient to propagate the wave energy at the global scale, it is usually not able to properly represent the physical processes that occur as the waves interact with shallow waters, such as refraction, depth induced breaking and bottom friction among others. Therefore, such wave data is not suitable for a proper assessment of the nearshore wave climate changes along different time slices and forcing scenarios, as well as the corresponding coastal impacts.

The present study aims to provide the first assessment of the projected nearshore changes in the wave climate of New Zealand, focussing on a range of time slices and RCP scenarios. We used the SWAN (Booij et al. 1999) wave model to downscale global WAVEWATCH III (WW3) simulations sourced from the COWCLIP project (Hemer et al. 2012). These wave simulations were run for three different models (ACCESS1.0, MIROC5 and CNRM-CM5), along three different time slices (1986–2005, 2026–2045 and 2081–2100) and two representative concentration pathways scenarios (RCP4.5 and RCP8.5). From the three models downscaled, the two best-performing models in the historic period (1986–2005) had their projections analysed whilst the third-performing model has been included in the supplementary material for the sake of completeness. Throughout the rest of the paper, the data and methods used in this study are described in Section 2, while our results are presented in Section 3. In Section 4 we discuss our findings and our final remarks are presented in Section 5.

2. Data and methods

2.1. Bathymetry

In order to properly resolve the physical processes that occur during the wave/bottom interaction in shallow waters, an accurate bathymetric database is required. We used a high-resolution (250 m) bathymetry provided by the National Institute of Water and Atmospheric Research (NIWA). This database was compiled from a series of multi- and single-beam data surveys carried out by NIWA, Land Information New Zealand (LINZ) and a number of international surveying vessels from countries such as the United States of America, France, Germany, Australia and Japan (Mitchell et al. 2012).

2.2. Historical wave hindcast

The wave climate database used in this study to estimate the GCM's uncertainties is a regional hindcast of the New Zealand area (20yhcast hereinafter), carried out by Albuquerque et al. (2021) and available at <https://coastalhub.science/data>. This database is a 20-year (1993–2012) SWAN simulation, forced with winds from the Climate Forecast System Reanalysis (CFSR), and multimodal spectral boundaries from a partitioned global wave hindcast, conducted by the Institut français de recherche pour l'exploitation de la mer (IFREMER) (Rascle et al. 2008; Ardhuin et al. 2011; Rascle and Ardhuin 2013), with the WW3 wave model (Tolman 2009). Each node/boundary point of the IFREMER hindcast contains estimated parameters of integrated wave height (H_s), energy period (T_e), mean direction (θ_m) and directional spread (σ_θ), plus partitioned parameters (H_{sn} , T_{pn} , θ_{pn} and $\sigma_{\theta pn}$, $\{n = 1, \dots, 6\}$), where the first partition ($n = 1$) describes wind-sea waves (regardless of whether these waves are available in a given sea state) and the next 5 represent the different swell systems (sorted by wave height) that may be present in the same sea state.

For all boundary points, the wave height of each WW3 partition was corrected according to the wave type (wind or swell), direction and the available satellite data, as per Albuquerque et al. (2018). The corrected wave partitions were used to reconstruct the multimodal wave spectra as described in Albuquerque et al. (2021) prior to the downscaling. The downscaled database (also available at <https://coastalhub.science/data>) provides an extensive list of integral and partitioned wave parameters, extending from (164.5° E, 50.0° S) to (181.0° E, 31.5° S) and constituting of a 4-level set of nested grids (28, 9, 3 and 1 km spatial resolution and 3-hourly output cycle) throughout New Zealand. Validation with the available buoys showed good agreement between the hindcast and in situ measurements, suggesting that this database is adequate for the comparison.

Other studies use more than one hindcast together with satellite data in order to estimate the uncertainty of the hindcast period as well. In the case of New Zealand, such an approach was discarded for three reasons: first, the wave height boundaries of our hindcast were previously corrected with satellite data as previously stated; second, from the two published regional wave hindcasts available, the one described in Gorman et al. (2003a 2003b) provides an overlap of only 5 years with the 20yhcast while the one used in Godoi et al. (2016) presents larger values of RMSE and negative bias compared to the 20yhcast, and; third, data from global hindcasts such as the ERA-Interim (Dee et al. 2011), used as reference hindcast in similar studies, are too coarse (grid resolution ~ 110 km) to properly represent the New Zealand area.

2.3. COWCLIP project wave simulations

During the first phase of the COWCLIP project (Hemer et al. 2012), wind forcings of the historic period (1986–2005) of twelve GCMs were used to conduct a series of near-global (latitude 80° S–80° N) 1° resolution wave simulations (Hemer and Trenham 2016). Under the second phase of the COWCLIP project, the twenty-first century's near-future (2026–2045) and end (2081–2100) time slices of these GCMs were simulated under two different RCP (4.5 and 8.5) scenarios (Morim et al. 2019).

The spectral domain of these simulations consisted of 24 directional bins and 25 frequencies ranging non-linearly from 0.04 to 0.5 Hz. The ST3 parametrization (Bidlot et al. 2007) was adopted to run the WW3 model. The results available consist of 6-hourly grids containing integrated parameters of H_s , T_m , f_p , θ_m and θ_p , as well as similar parameters for wind-sea and swell waves.

2.4. Model selection and boundary forcings

Given the wide range of global wave simulations forced by GCMs available, their different time slices and scenarios, choosing a set of models to downscale can easily become an issue regarding computational and storage resources. In the present study, the downscaling of each selected GCM unfolds in five different simulations (historic period, near-future and end of twenty-first century, the latter two under RCPs 4.5 and 8.5). With that in mind, our approach was to restrict the simulations to the three models that better represent the atmospheric patterns that generate the waves around New Zealand.

Atmospheric parameters of sea level pressure fields (SLP) have been extensively used in statistical downscaling (SD) studies to predict the wave climate at the regional scale, including the New Zealand waters (Rueda et al. 2019). An SD study regarding storm surge projections (Cagigal et al. 2020) assessed and ranked (Perez et al. 2014) 39 GCMs based on their skill in representing SLP patterns around New Zealand. From the top five performing models (ACCESS1.0, EC-EARTH, MRI-ESMI, MIROC5, CNRM-CM5 respectively), we chose the top three ranked models that had boundary forcings available from the COWCLIP project, i.e. ACCESS1.0, MIROC5 and CNRM-CM5. The details of the selected models are shown in Table 1.

2.5. Spectral reconstruction

Minding how limited the unimodal spectrum is in representing the wave parameters in areas such as New Zealand (Albuquerque et al. 2021), and the potential implications of such limitations when estimating uncertainty between the downscaled GCMs waves and

Table 1. Names and spatial resolution of the CMIP5 GCMs used for wave and wind forcings in this study.

Model	Full model name	Atm. res. (lon, lat)
ACCESS1.0	Australian Community Climate and Earth System Simulator 1.0	1.88 × 1.25
CNRM-CM5	Centre National de Recherches Meteorologiques Coupled Global Climate Model, ver. 5	1.4 × 1.4
MIROC5	Model for Interdisciplinary Research on Climate, version 5	1.4 × 1.4

our hindcast, we reconstructed the spectral boundary forcings with all the information of wind-sea and swell waves available in COWCLIP. Among the wave parameters provided in the WW3 projections, we used the estimations of significant wave height, peak period and peak direction for bulk parameters, as well as significant wave height and peak period of wind-seas and swells ($H_{s(sea/swell)}$, $T_{p(sea/swell)}$) and mean direction of wind-seas ($\theta_{m(sea)}$).

The wind-sea fraction of the reconstructed wave spectra was based on $H_{s(sea)}$, $T_{p(sea)}$ and $\theta_{m(sea)}$, as we assumed $\theta_{m(sea)} \approx \theta_{p(sea)}$. For swells, we used $H_{s(swel)}$, $T_{p(swel)}$, and estimated the peak swell direction as the vector difference between the integrated peak direction and the wind-sea mean direction (Equation (1)).

$$\theta_{p(swel)} = \arctan\left(\frac{H_s^2 \cdot T_p \cdot \sin(\theta_p) - H_{s(sea)}^2 \cdot T_{p(sea)} \cdot \sin(\theta_{m(sea)})}{H_s^2 \cdot T_p \cdot \cos(\theta_p) - H_{s(sea)}^2 \cdot T_{p(sea)} \cdot \cos(\theta_{m(sea)})}\right) \quad (1)$$

The wave spectrum was reconstructed using the JONSWAP spectral formulation (Haselmann et al. 1973), with peak enhancement factor (γ) calculated based on the wave height and peak period as per Torsethaugen et al. (1984); Haver and Nyhus (1986) for each partition, and the default peak-width (σ) parameter values (i.e. $\sigma_a = 0.07$ and $\sigma_b = 0.09$). The resulting two-dimensional spectrum consisted of 40 frequencies non-linearly distributed from 0.03 to 1.0 Hz, and 72 directional bins of 5° .

2.5.1. Directional spread

The spectral reconstruction process also required values of directional spread (σ_θ), which are not available within the COWCLIP wave parameters. In this study, we estimated the directional spread values using a k -NN regressor (Altman 1992), which works in two steps: training and predicting. During the training phase, a m -dimensional space is defined based on m arrays of features related to an array of elements. In the predicting step, m features are provided to the model, defining a position p in the m -dimensional space. The model then estimates the predicted element by averaging the k nearest neighbours (elements) from p in the m -dimensional space.

The approach we adopted uses the k -NN regressor relying on the relationship between f/f_p and σ_θ (Figure 1A and D) as in previous studies (Forristall and Ewans 1998; Ewans 2001), but without setting a minimum wave height threshold and instead, using the H_s values as an additional feature when defining the directional spread values position in the regressor's m -dimensional space. In order to calculate such values for wind-sea and swell waves for our training dataset, we used estimated H_{sn} , T_{pn} and $\sigma_{\theta n}$ from the corrected boundary points of the IFREMER hindcast. These boundary forcings were preferred over the 20yhcast data in order to use wind-sea and swell waves of similar characteristics, as SWAN and WW3 have different physics. The f/f_p value was defined by calculating the integrated value of T_{m01} from the available partitions and dividing the partition's peak period by the integrated mean period (T_{pn}/T_{m01}). Values from partition $p1$ were used to train the wind-sea waves regressor whilst the swell waves regressor was trained with values from the swell partitions ($p2$ to $p6$). For the prediction dataset, derived from the COWCLIP WW3 boundaries, the values were gathered in a similar way, however without the need of calculating T_{m01} and using only two partitions (wind-sea or swell) to calculate f/f_p and establish its relationship with H_s . The prediction dataset of wind-sea and swell waves were then used as input to the k -NN regressors,

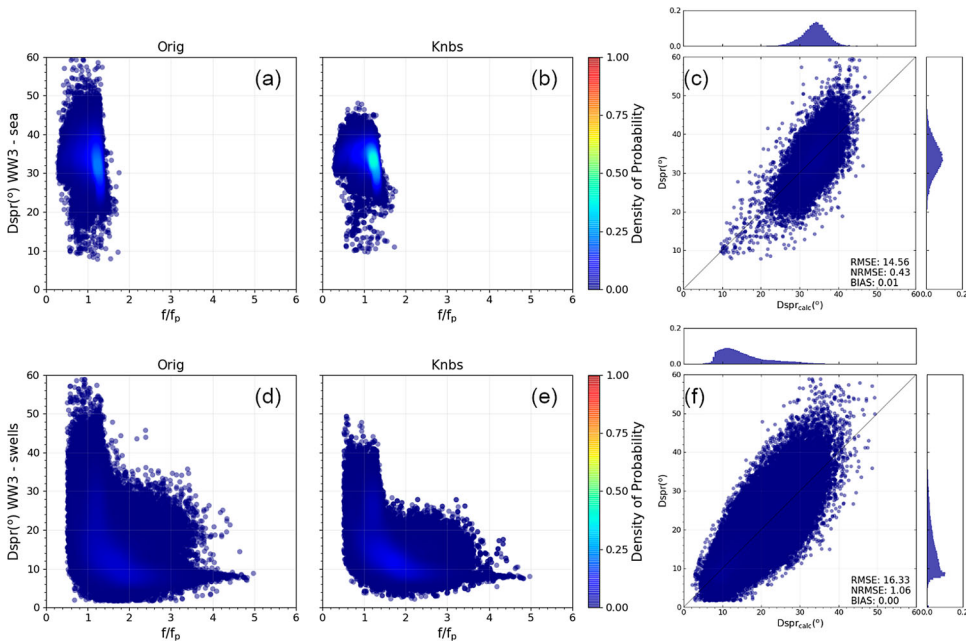


Figure 1. Relationship between σ_θ (y-axis) and f/f_p (x-axis) for the WW3 data and the k -NN regressor values for sea (A, B) and swell (D, E) waves. Scatterplots comparing the values of σ_θ from WW3 (y-axis) and from the k -NN regressor (x-axis) for seas (C) and swells (F). Colorbar shows the density of probability of the scatters in figures A, B, D and E while histograms show the probability density function of the parameter in the respective axis of figures C and F.

which provided, for each pair of $(H_s, f/f_p)$, a value of directional spread averaged between the $k = 3$ nearest neighbours found in the regressor's m -dimensional space. Our estimated values of σ_θ can be seen in Figure 1, where the first column shows the σ_θ values from WW3, the second column shows the σ_θ values from the k -NN regressor, and the third column shows the comparison between the values of directional spread from WW3 and the k -NN regressor. Higher values of k resulted in a narrower distribution of values for σ_θ .

2.6. Downscaling

Winds have a strong influence over ocean waves. Hence, in order to account for their effects regarding wave generation and propagation along our regional grids, the original winds of each model, time slice and RCP scenario were used in our downscaling. Whilst in terms of time all models share the same 3-hourly resolution, the ACCESS1.0 model provides wind fields within a spatial resolution (lon, lat) of $1.25^\circ \times 1.875^\circ$, while the CNRM-CM5 and MIROC-5 models atmospheric resolution is approximately $1.4^\circ \times 1.4^\circ$. The wind fields of each model were interpolated into the grid resolution for the wave downscaling.

The winds and bimodal boundary forcings described in the previous sections were used to downscale a 4-level nesting (28, 9, 3 and 1 km) set of grids (Figure 2, 3 km grids were omitted for the sake of simplicity). The outermost grid (28 km) was used to

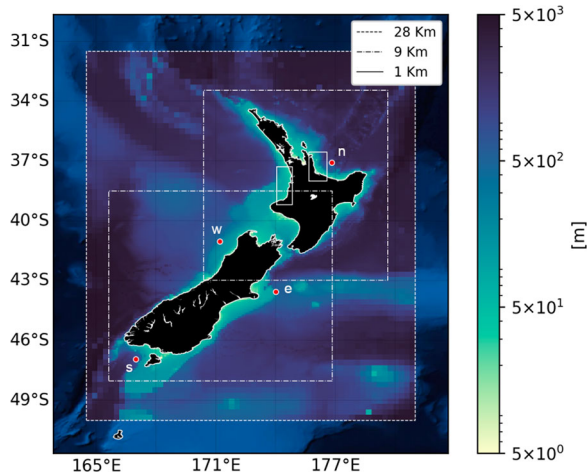


Figure 2. Grids and bathymetry used in this study. Dashed lines indicate 28 km resolution grid for the whole New Zealand, dot-dashed lines indicate 9 km resolution grids for North Island and South Island and solid lines show the 1 km grids. Resolution of image within each grid corresponds to the actual bathymetric resolution. Colors represent the depth as per colorbar. Red dots indicate the locations where the time series of data were analysed.

produce uniform conditions of spectral propagation from the outer boundaries to the 9 km grids, in order to minimise the bias on the estimated parameters along the overlapping areas of these grids. Intermediary 3 km spatial resolution grids were nested between the 9 and 1 km grids in order to better resolve the nearshore processes in shallower waters without adding much to the total computational effort. Finally, the 1 km grids were downscaled to assist the nearshore studies of three different areas: Raglan, on the west coast of New Zealand; Tairua and Tauranga, both along the northeast coast of the country. While we downscaled 20-year GCM-forced wave simulations for projected and historic time slices, there is only a 13-year overlap (1993–2005) between the GCM historical experiment (1986–2005) and the 20yhcast (1993–2012).

The spectral space consisted of 72 directions and 34 frequencies exponentially distributed from 0.03 to 1.0 Hz. A cut-off frequency of 0.5 Hz was applied to the model's output following the same standard adopted in the reference hindcast. Each 20-year simulation was run as 40 'embarrassingly parallel' (each SWAN run was able to perform its own computations independently of the previous run's results) 6-month non-stationary SWAN runs. In order to achieve this, a stationary computation was employed to propagate the initial wave condition (i.e. first time-step of boundary conditions) of the first 6-month non-stationary simulation. The other 39 runs were started 36 simulation-hours earlier than their first output cycle, allowing the wave energy to propagate towards the whole grid. This approach allowed for homogeneous transitions between the results (at the same simulation time) at the beginning of a simulation and the end of the previous one, regardless of the order they were computed. The same technique was applied to the nested grids, however, each of these simulations was still dependent on the run of their 'parent' grid. Each simulation results were stored as integrated and partitioned wave parameters. In total, the historic period + 2 time slices \times 2 RCPs \times 3 models were computed, resulting in 300 simulation years, divided in 6-monthly runs of 7 different grids, that is, 4200 SWAN runs.

2.7. Assessments of historic bias and projected changes

The assessment of the historic bias between GCMs and the 20yhcast included the full 20-year time slices of the datasets. We ignored the time slice mismatch as the internal variations of the GCMs are not expected to occur at the same time as those found in observations (Taylor et al. 2012), and considered the GCMs as being representative of the wave climate regardless of the period in time (Semedo et al. 2012). We assumed that the differences between the 20yhcast and the GCMs are not caused by the non-stationarity of the wave climate, but by model and observation biases (Hemer et al. 2013).

The skill of the GCMs historic wave simulations was assessed in three ways. First, we calculated the spatial percentage mean bias error (pmbe, here defined as $100 \times (\text{GCM}_{\text{hist}} - 20\text{yhcast}) / 20\text{yhcast}$) of yearly and seasonal mean wave parameters – except for θ_p , which bias was calculated as $\text{GCM}_{\text{hist}} - 20\text{yhcast}$. Second, we quantified the spatial biases between GCMs and the reference hindcast by calculating the Pearson's correlation coefficient (r), root mean squared error (rmse), normalised mean squared error (nrmse), bias and pmbe between the grid nodes of the GCMs and the 20yhcast, for annual and seasonal means. Third, we assessed the bias between hindcast's and GCMs' cumulative distributions of wave height at four different locations (points w: 171.195° E, 41.021° S, n: 176.809° E, 37.083° S, e: 174.002° E, 43.552° S and s: 166.985° E, 46.927° S, Figure 2) along New Zealand's west, north, east and south coasts.

The spatial pmbe analysis was conducted for wave parameters of height, as well as its 99th percentile, and peak period (for peak direction we calculated bias). The other statistics were calculated and summarised for H_s , T_p and θ_p , whilst the cumulative distribution bias between GCMs and the 20yhcast was calculated for significant wave height.

For the projected wave climate, the two best-performing models in the historic simulation were analysed. The analysis consisted of using the spatial percentage mean bias error to measure the changes in wave height and period, and the absolute bias to measure the change in wave direction between the historical and projected periods. The statistical significance of the projected changes was calculated using a two-tailed Welch's t-test. We produced a summary of the projected changes at sites w, n, e and s, and calculated the return period of H_s extreme events for all time slices and RCPs by fitting a General Pareto Distribution (GPD) to the values obtained by a peak over threshold (POT) method. The storm definition criteria used in the extreme event analysis is based on Méndez et al. (2006) and accounted for events of wave height larger than the 99th percentile with a duration of at least 3 hours and a 72-hour independence between peaks.

3. Results

3.1. Historic period: hindcast vs GCM-forced simulations

Figure 3 displays the 20yhcast annual and seasonal mean wave heights on the top left plot, and the mean annual and seasonal percentage mean bias error in H_s between the ACCESS1.0 (top right), MIROC-5 (bottom left) and CNRM-CM5 (bottom right) models. The ACCESS1.0 model shows an annual pmbe ranging around 15% on most of the offshore areas, increasing towards the shore (20%–25%) and reaching up to 35% within the Cook Strait area. Seasonality shows similar spatial patterns of pmbe, with the differences being

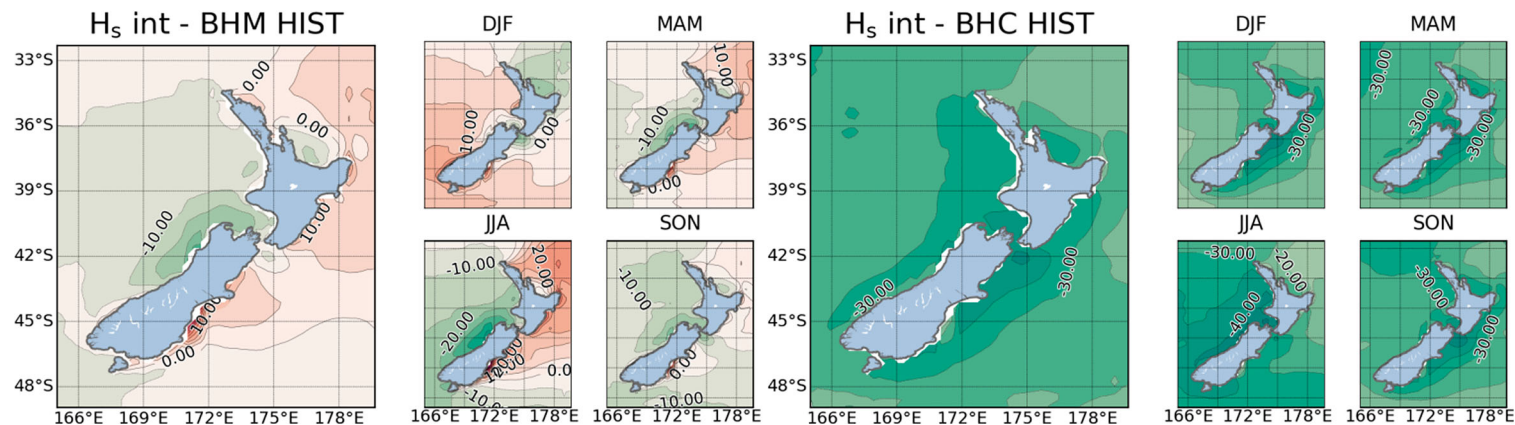
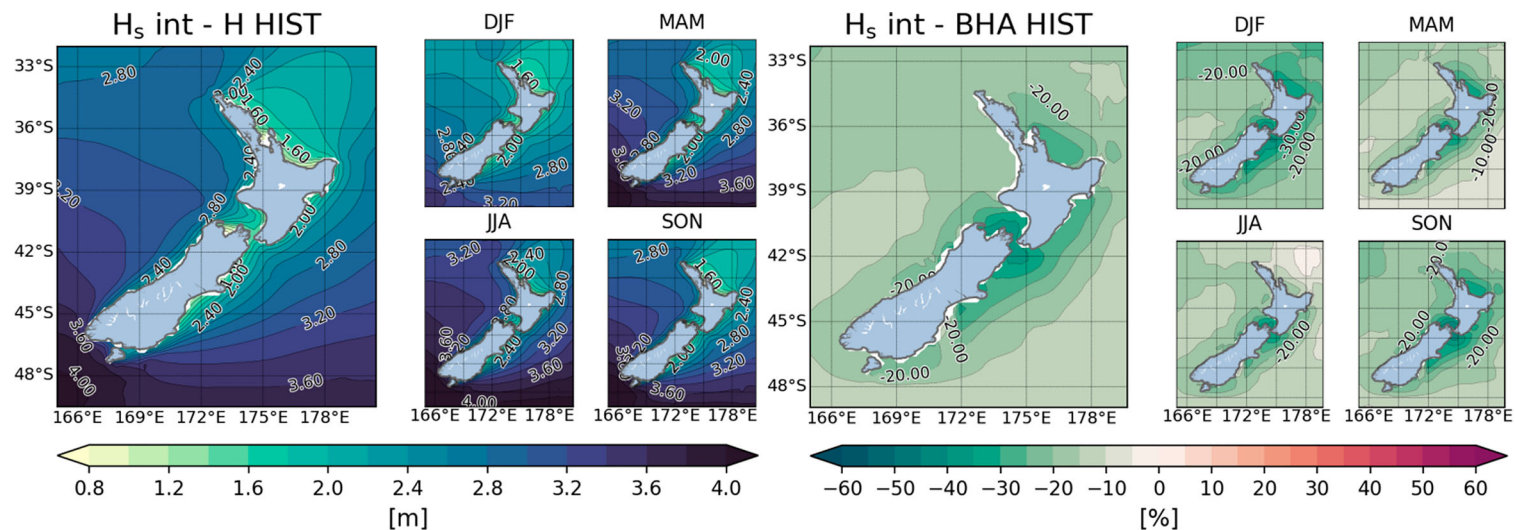


Figure 3. Annual (large panel) and seasonal (small panels) H_s means of the 20yhcst (top left) and normalised bias in mean H_s between the 20yhcst and the historical period of the ACCESS1.0 (top right), MIROC-5 (bottom left) and CNRM-CM5 (bottom right) models. Austral summer, autumn, winter and spring are indicated by DJF, MAM, JJA and SON respectively, wave height values for the 20yhcst are shown in the top left colorbar. Top right colorbar indicates the normalised bias values for all the three models.

larger during (austral) spring (September, October and November – SON) and summer (December, January and February – DJF) months, and smaller during autumn (March, April, May – MAM) and winter (June, July and August – JJA) months. MIROC-5 shows a H_s pmbe ranging from approximately $\pm 5\%$ to $\pm 20\%$, the lowest values within the offshore areas, and the largest values around the west and east coasts of the South Island. Overall, the H_s values are over estimated along the north and east and under estimated along the west and south of the domain. Seasonality shows a similar pattern, with different values during autumn, winter and spring, as well as an inverse pattern in the summer months. CNRM-CM5 (bottom right plot of [Figure 3](#)) exhibits the largest pmbe in mean H_s , from nearly -20% offshore of New Zealand to -40% along the nearshore, with larger values near the Cook Strait for yearly H_s . Seasonal values show small changes compared to the annual mean.

With regards to the mean of H_s^{99} events, [Figure 4](#) shows the 20yhcast's annual and seasonal values on the top left plot. The percentage mean bias error in H_s^{99} observed for ACCESS1.0 (top right plot) has similar annual spatial patterns compared to its mean H_s ([Figure 3](#)), but with lower values (10% along the west and northeast coasts, and 5% along the southeast coast). Seasonality shows spatial patterns similar to the H_s pmbe on summer and autumn (the latter having the lowest pmbe), and different patterns during winter and spring. For MIROC-5 (bottom left plot), the pmbe shows over (under) estimation of up to 15% (-20%) in H_s^{99} along the northeast of the domain (northwest of the South Island). Seasonal H_s^{99} patterns are similar to H_s , but with moderately different pmbe values. Finally, CNRM-CM5 (bottom right of [Figure 4](#)) is the most biased model for H_s^{99} . The model under predicts the extreme events of wave height from nearly -20% (northwest of the domain) to about -40% (along the west and southeast coasts). Compared to H_s , seasonality shows larger pmbe for extreme events, and similar spatial patterns during autumn, winter and spring.

Annual and seasonal peak period values of the 20yhcast are shown in the top left plot of [Figure 5](#). Percentage mean bias error in T_p of the ACCESS1.0 model (top right plot) is around -5% through most of the domain, decreasing along the west and east coasts, and increasing to -12% along the northeast coast. The Cook Strait area shows positive pmbe of up to 10%. Seasonal pmbe is the largest during summer and the lowest in spring months, while the negative pmbe observed along the northeast coast is not present during winter. For MIROC-5 (bottom left plot of [Figure 5](#)), T_p is under estimated to the south (approximately -2%) and west (-4%) of the domain, and over estimated (up to 16%) along the east, northeast and Cook Strait areas. Summer months show lower positive pmbe off the west and east coasts, and negative pmbe along the northeast coast. Regarding the remaining seasons, pmbe increases progressively in autumn, spring and winter, the latter showing the largest (positive and negative) percentage mean bias error. CNRM-CM5 (bottom right plot) shows under estimation of T_p through the whole domain, with values of -18% , -16% and -12% off the west, east and northeast coasts respectively, decreasing shorewards along the west and east of New Zealand. Seasonality shows increasing pmbe (under estimation) from summer to winter, decreasing in spring. Winter months also show the lowest pmbe along the northeast coast.

Mean annual and seasonal θ_p calculated from the 20yhcast are presented in the top left plot of [Figure 6](#). Peak wave direction of the ACCESS1.0 model ([Figure 6](#), top right) is biased by about 6° (clockwise) off the west coast, decreasing to 2° along the nearshore.

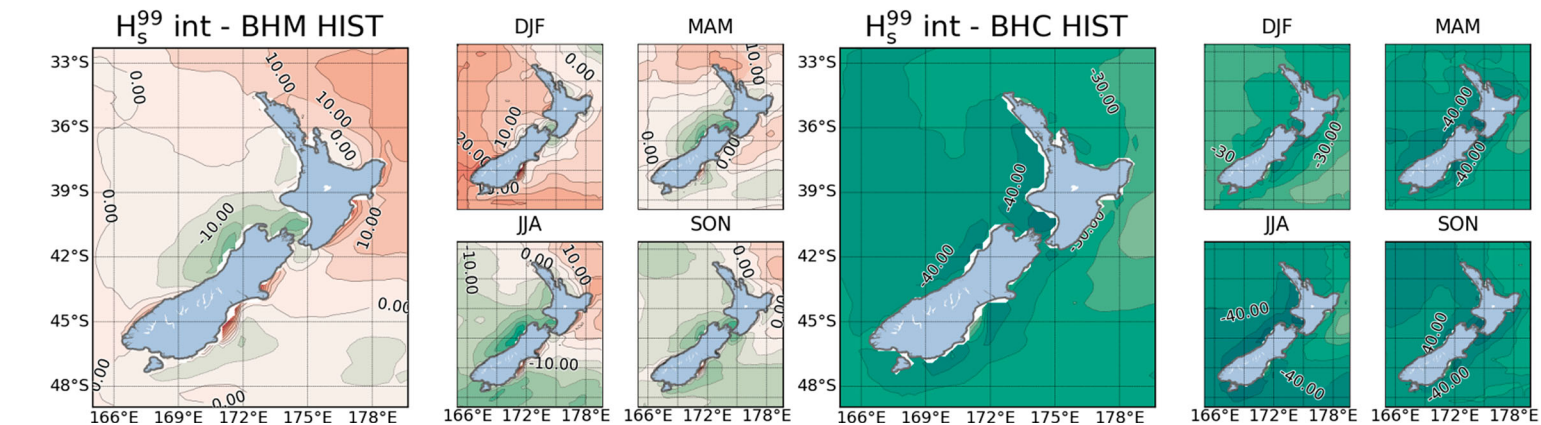
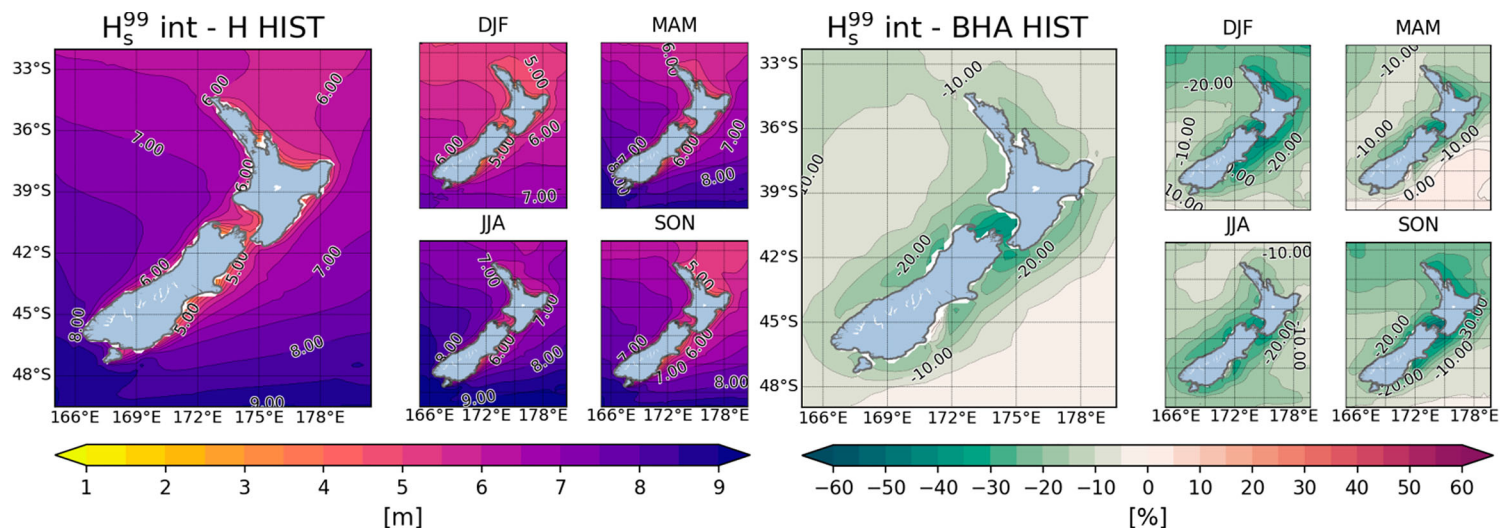


Figure 4. Annual (large panel) and seasonal (small panels) H_s^{99} means of the 20yrcast (top left) and normalised bias in mean H_s^{99} between the 20yrcast and the historical period of the ACCESS1.0 (top right), MIROC-5 (bottom left) and CNRM-CM5 (bottom right) models. Austral summer, autumn, winter and spring are indicated by DJF, MAM, JJA and SON respectively, H_s^{99} values for the 20yrcast are shown in the top left colorbar. Top right colorbar indicates the normalised bias values for all the three models.

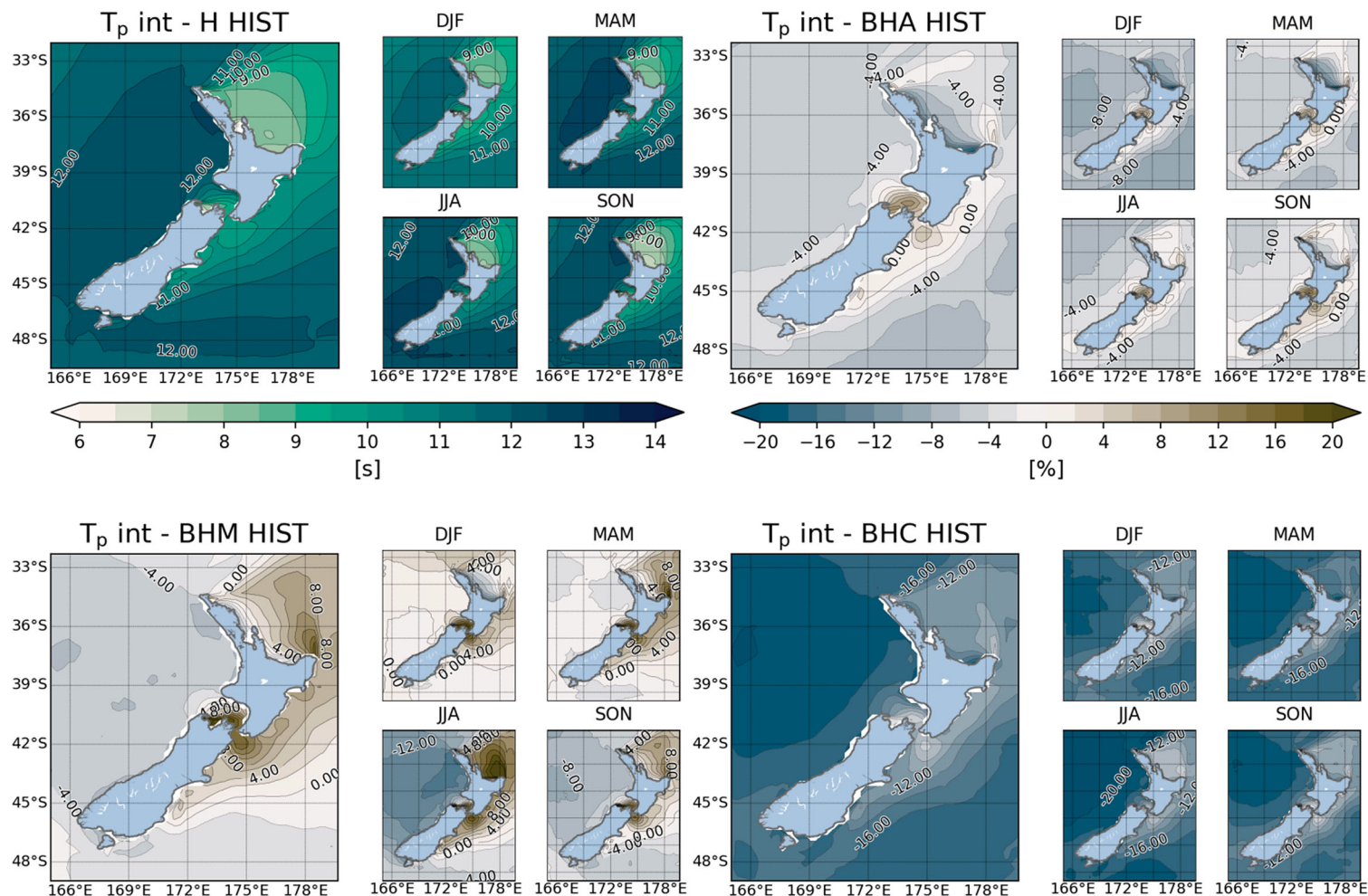


Figure 5. Annual (large panel) and seasonal (small panels) T_p means of the 20yhcst (top left) and normalised bias in mean T_p between the 20yhcst and the historical period of the ACCESS1.0 (top right), MIROC-5 (bottom left) and CNRM-CM5 (bottom right) models. Austral summer, autumn, winter and spring are indicated by DJF, MAM, JJA and SON respectively, T_p values for the 20yhcst are shown in the top left colorbar. Top right colorbar indicates the normalised bias values for all the three models.

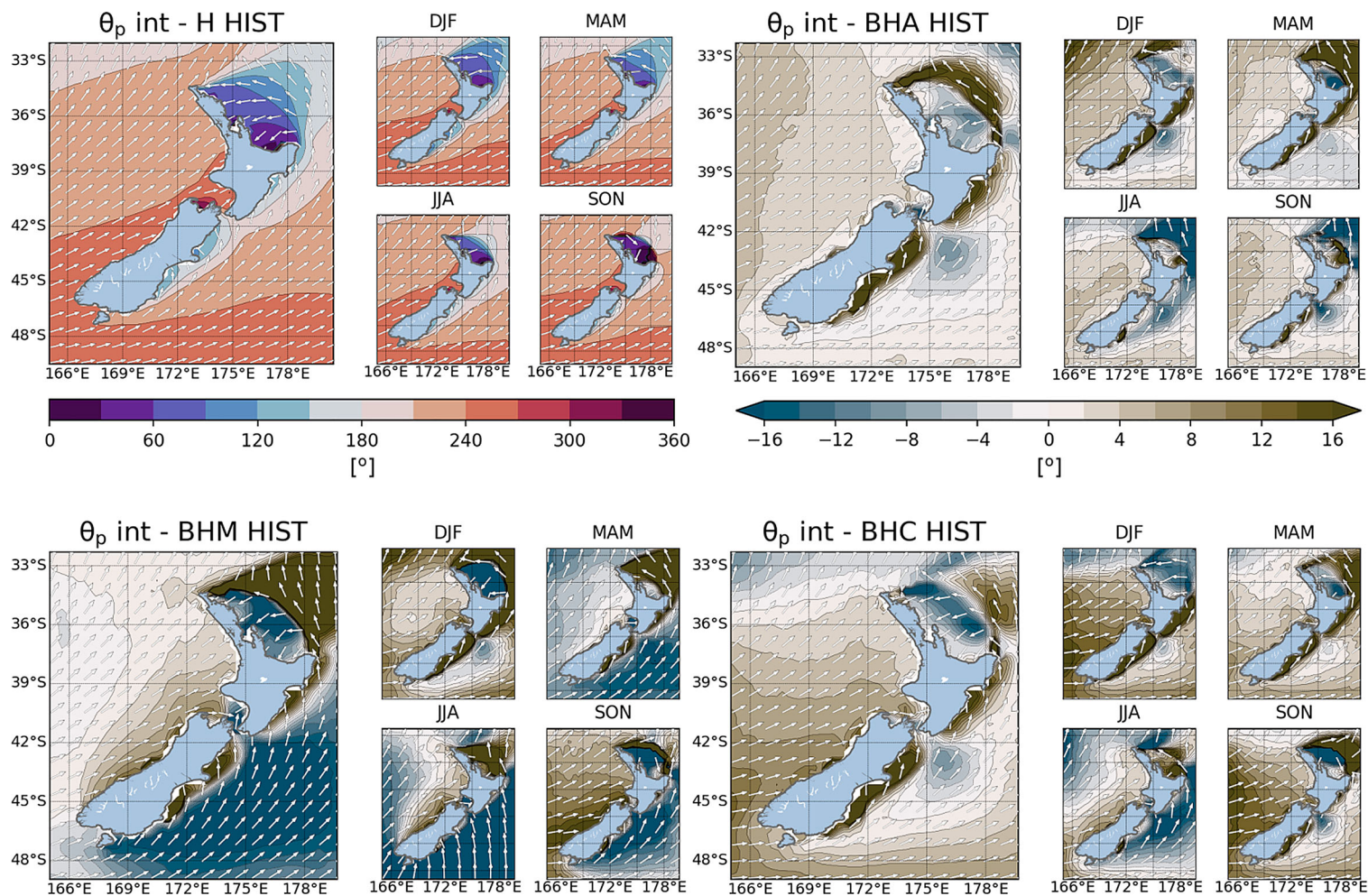


Figure 6. Annual (large panel) and seasonal (small panels) θ_p means of the 20yhcst (top left) and normalised bias in mean θ_p between the 20yhcst and the historical period of the ACCESS1.0 (top right), MIROC-5 (bottom left) and CNRM-CM5 (bottom right) models. Austral summer, autumn, winter and spring are indicated by DJF, MAM, JJA and SON respectively, θ_p values for the 20yhcst are shown in the top left colorbar. Top right colorbar indicates the bias values in degrees for all the three models.

Offshore of the east coast, the bias is small (2°), increasing to $> 16^\circ$ by the North and South islands coasts, whereas the area to the east of the Cook Strait shows a negative (anti-clockwise) bias of -10° . The northeast coast has the most complex spatial bias, which is negative along the nearshore (-2° to -10°) and the northwest of the domain (-10°), with an arch of positive values ($> 16^\circ$) stretching from Cape Reinga to East Cape (the west- and eastmost points of the northeast coast). Along the west of the domain, seasonal variability shows the same pattern of positive bias, the largest values during summer and an area of negative bias towards the north during winter. Along the east, we see the same pattern observed in the annual mean, with a large reduction of the positive bias along the coast and an increase of the negative bias east of the Cook Strait during winter. For the northeast coast, the positive and negative biases change, with the negative (positive) bias present along most of the nearshore (offshore) areas in summer and spring, this pattern inverts during winter and autumn. The MIROC-5 model is the most biased with regards to θ_p , along most of the east (larger than $\pm 16^\circ$, positive along the nearshore, negative offshore) and northeast (larger than $\pm 16^\circ$, negative along the nearshore, positive offshore) coasts. Along the west, bias is negative (approximately -2°) offshore, increasing shorewards to 4° – 6° along the North Island, and up to 10° – 12° along the South Island. Seasonal means of θ_p show similar patterns of positive and negative bias during autumn and winter (with different spatial distributions). Summer and winter show different patterns of positive bias along most of the west and northeast, whereas the bias along the east coast is mostly positive during summer and mostly negative during spring. CNRM-CM5 values of θ_p are the best results this model produced within the analysed variables. Bias is positive along most of the domain, starting at 12° southwest of the domain, progressively decreasing northwards along the west coast and becoming negative to the north of the domain. Along the east, the bias is positive (10°) along the south, increasing towards the nearshore ($> 16^\circ$) of both islands, and negative southeast of the Cook Strait. The northeast of the domain shows negative bias along the nearshore and positive bias off the coast. This pattern is also visible (with noticeable differences) during summer, spring and autumn. During winter, the bias is mostly negative off (positive along) the west and east coasts, and mostly positive along the northeast coast.

3.1.1. Historic period bias summary

Statistics of r , rmse, nrmse bias and pmbe were calculated by comparing each grid cell of the annual and seasonal means of the ACCESS1.0, MIROC-5 and CNRM-CM5 models against the correspondent grid cell of the 20yhcst (note that the normalised statistics were not calculated for θ_p). Results of the annual means (Table 2) show the ACCESS1.0 model as the best-performing model in terms of r for all wave parameters analysed (followed by CNRM-CM5), and the best-performing model regarding wave direction. MIROC-5 is the best model for H_s and T_p for all the remaining statistics (followed by ACCESS1.0), yet it performs poorly on θ_p , showing the smallest r and the largest rmse for this parameter.

The seasonal variability of these statistics (Table 3) shows results similar to the annual means (in terms of model skill) for H_s the whole year round, and for T_p during summer and autumn. ACCESS1.0 is the best-performing model regarding T_p during winter and spring, as well as θ_p during summer and winter. In autumn and spring, bias in θ_p is the

Table 2. Comparison between annual mean values of the ACCESS1.0 (A), MIROC-5 (M) and CNRM-CM5 (C) GCMs, and the reference hindcast for the historic period.

Model	H_s					T_p					θ_p		
	<i>r</i>	rmse	nrmse	bias	pmbe	<i>r</i>	rmse	nrmse	bias	pmbe	<i>r</i>	rmse	bias
A	0.989	0.486	0.168	-0.478	-0.165	0.976	0.576	0.051	-0.514	-0.045	0.980	5.964	2.266
M	0.961	0.184	0.063	-0.077	-0.027	0.924	0.552	0.048	-0.190	-0.017	0.919	13.381	-2.425
C	0.982	0.831	0.287	-0.813	-0.281	0.961	1.899	0.167	-1.840	-0.162	0.972	7.284	3.235

Note: Rows display each model, columns show statistics for each wave parameter analysed. Values in bold indicate the best agreement between models and hindcast.

Table 3. Comparison between seasonal mean values of the ACCESS1.0 (A), MIROC-5 (M) and CNRM-CM5 (C) GCMs, and the reference hindcast for the historic period.

Model	H_s					T_p					θ_p		
	<i>r</i>	rmse	nrmse	bias	pmbe	<i>r</i>	rmse	nrmse	bias	pmbe	<i>r</i>	rmse	bias
summer – DJF													
A	0.985	0.517	0.210	-0.510	-0.207	0.959	0.801	0.074	-0.751	-0.070	0.974	9.245	4.258
M	0.980	0.235	0.095	0.129	-0.052	0.941	0.347	0.032	0.120	-0.011	0.909	18.344	8.368
C	0.982	0.618	0.250	-0.610	-0.247	0.958	1.683	0.156	-1.633	-0.152	0.961	11.660	5.172
autumn – MAM													
A	0.990	0.413	0.140	-0.403	-0.136	0.971	0.572	0.049	-0.498	-0.043	0.971	11.110	4.291
M	0.945	0.204	0.069	-0.025	-0.008	0.940	0.440	0.038	0.076	-0.007	0.963	12.344	-4.304
C	0.983	0.818	0.277	-0.803	-0.272	0.969	1.977	0.169	-1.934	-0.166	0.975	8.839	4.707
winter – JJA													
A	0.972	0.495	0.153	-0.472	-0.146	0.971	0.568	0.048	-0.487	-0.042	0.963	9.388	-1.620
M	0.680	0.472	0.146	-0.174	-0.054	0.481	1.159	0.099	-0.554	-0.047	0.466	36.219	-20.055
C	0.904	1.070	0.331	-1.023	-0.317	0.916	2.123	0.181	-2.037	-0.174	0.948	9.728	-3.144
spring – SON													
A	0.990	0.535	0.183	-0.527	-0.180	0.977	0.430	0.038	-0.323	-0.028	0.943	8.689	0.301
M	0.981	0.288	0.098	-0.236	-0.080	0.946	0.678	0.060	-0.398	-0.035	0.801	16.490	0.199
C	0.987	0.828	0.283	-0.814	-0.278	0.965	1.822	0.160	-1.750	-0.154	0.836	16.155	6.642

Note: Rows display each model, columns show statistics for each wave parameter analysed. Values in bold indicate the best agreement between models and hindcast.

smallest for ACCESS1.0 and MIROC-5 respectively, whereas *r* and rmse are best for CNRM-CM5 and ACCESS1.0 correspondingly during these seasons.

Biases between observed and modelled cumulative distributions at sites w, n, e and s (Figure 7) show a general under estimation of H_s by the three GCMs. ACCESS1.0 and CNRM-CM5 under estimate both the upper and lower tails of the distribution at all

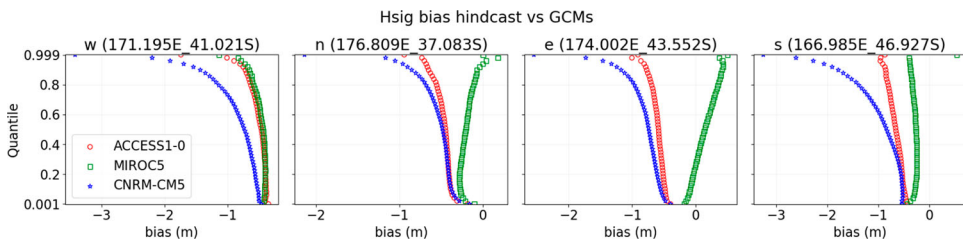


Figure 7. Quantile–quantile bias in significant wave height between the tree GCMs and the reference hindcast (GCM – 20yhcast) at sites w (171.195° E, 41.021° S), n (176.809° E, 37.083° S), e (174.002° E, 43.552° S) and s (166.985° E, 46.927° S). Vertical and horizontal axes show the quantiles and model bias in metres, respectively.

locations, whilst MIROC-5 partially over estimates the distribution at sites n (upper tail) and e (above the 20th percentile).

In summary, the ACCESS1.0 and MIROC-5 models are more accurate in representing the H_s and T_p parameters. For θ_p , ACCESS1.0 is the most accurate, followed by CNRM-CM5. In terms of cumulative distributions of significant wave height, MIROC-5 is the less biased model at the locations analysed, followed by ACCESS1.0 and CNRM-CM5. These results allow us to define MIROC-5 and ACCESS1.0 as the two most skilled models, followed by CNRM-CM5.

3.2. NEA21C projections

Projected changes between the historic and projected periods of the ACCESS1.0 and MIROC-5 models for the twenty-first-century near-future (2026–2045), RCPs 4.5 and 8.5 are displayed in Figures 8 to 11. Changes projected for annual mean H_s of the ACCESS1.0 model (left plots of Figure 8) shows small values ($< \pm 5\%$) and slight differences between RCP4.5 (Figure 8, top plots) and RCP8.5 (Figure 8, bottom plots). The change is positive along the west coast and off the east coast, and negative along the east coasts and northeast of the domain. Seasonal means show larger positive change ($>5\%$) during spring along (and off) most of the west and east coasts for both RCPs. During summer and winter, a larger positive change ($>5\%$) is observed for RCP4.5, as well as larger areas where the projected change is negative along the northeast coast for RCP8.5. Although the areas of statistically significant changes (marked with dots) are not very large for annual means, such areas are remarkably large on the seasonal means, particularly for RCP4.5. The spring months show the largest areas of significant changes in both RCPs.

For MIROC-5 (right plots of Figure 8), the change projected for annual H_s follows the same pattern, i.e. positive along the west and negative along the east coasts (also $< \pm 5\%$), but with larger positive change ($>5\%$), as well as areas of statistical significance in RCP8.5 (Figure 8, bottom left plots). Seasonal plots show a larger negative change (10%) in autumn and a larger positive change in summer (northeast coast) for RCP4.5 (Figure 8, top left plots), whereas larger areas of positive change are present in winter and spring on RCP8.5. Likewise ACCESS1.0, for MIROC-5 the areas of statistical significance are larger during spring for both RCP scenarios.

Projected changes for mean annual H_s^{99} (Figure 9) show a general increase in extreme wave heights along the west and southeast coasts, and mostly a decrease along the northeast coast (change ranging up to $\pm 10\%$), for both models and RCPs. Statistically significant changes are present along the southwest coast for the two models (both RCPs), and along the northeast coast for both models in RCP4.5, nearshore for ACCESS1.0, offshore for MIROC-5. Seasonality shows both models agreeing on a statistically significant increase in H_s^{99} along the west and southeast of the domain in winter and spring, and a decrease in H_s^{99} along the northeast in summer and autumn, for RCP4.5 and RCP8.5. The main areas of inter-model disagreement occur southeast of the domain, in autumn (RCP4.5).

Projections of T_p show the same pattern of increasing projected changes along the west and decreasing along the east/northeast (from -2% to 4% , Figure 10). The expected change of annual T_p means is smaller for ACCESS1.0 (left plots of Figure 10) than for

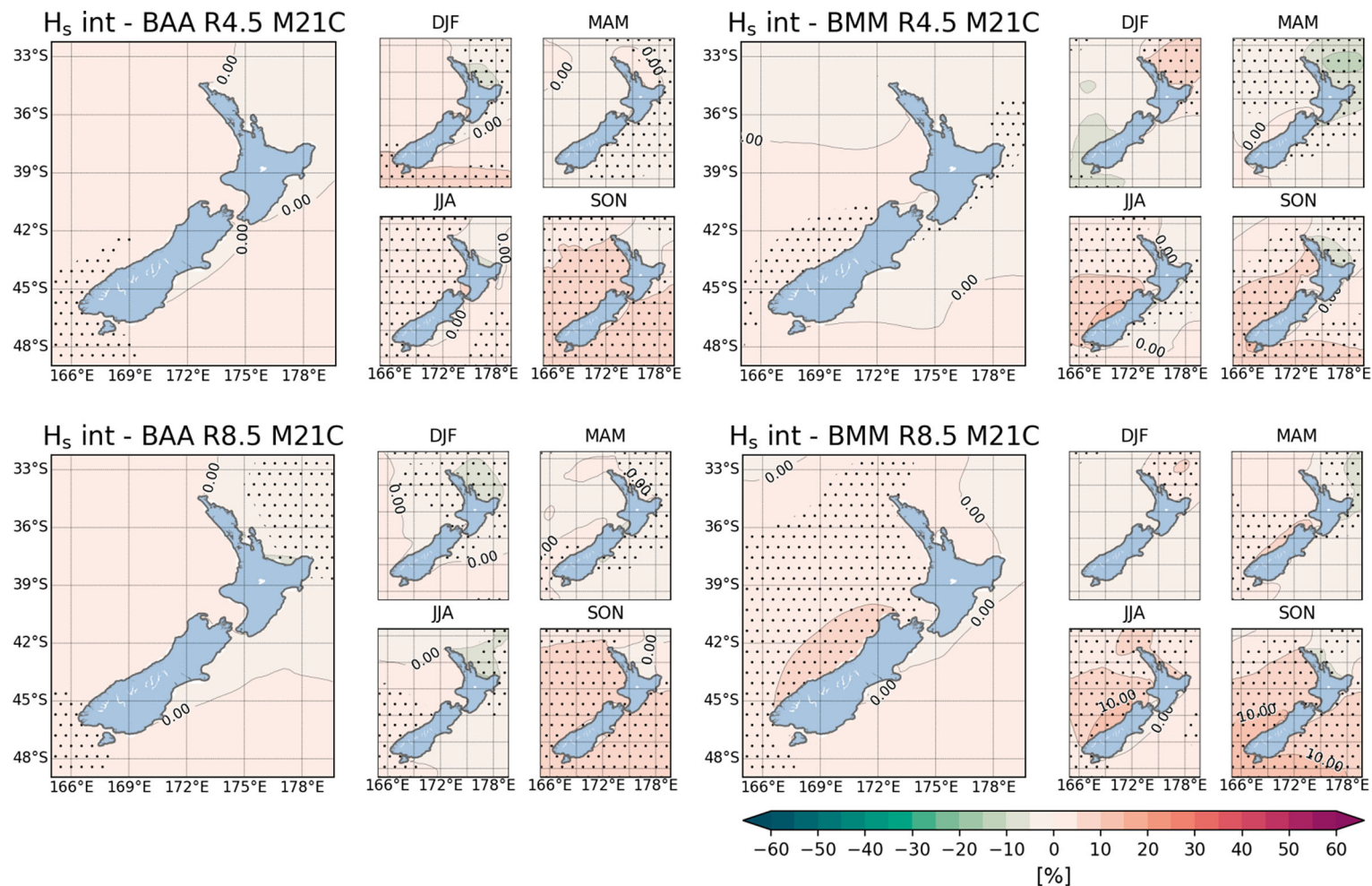


Figure 8. Annual (large panel) and seasonal (small panels) normalised H_s bias between the historic and projected (MID21C) periods of the ACCESS1.0 (right plots) and MIROC-5 (left plots) models, for RCPs 4.5 (top plots) and 8.5 (bottom plots). Austral summer, autumn, winter and spring are indicated by DJF, MAM, JJA and SON respectively. Bottom left colorbar indicates the normalised bias values between the time slices and the dots mark areas where changes are statistically significant.

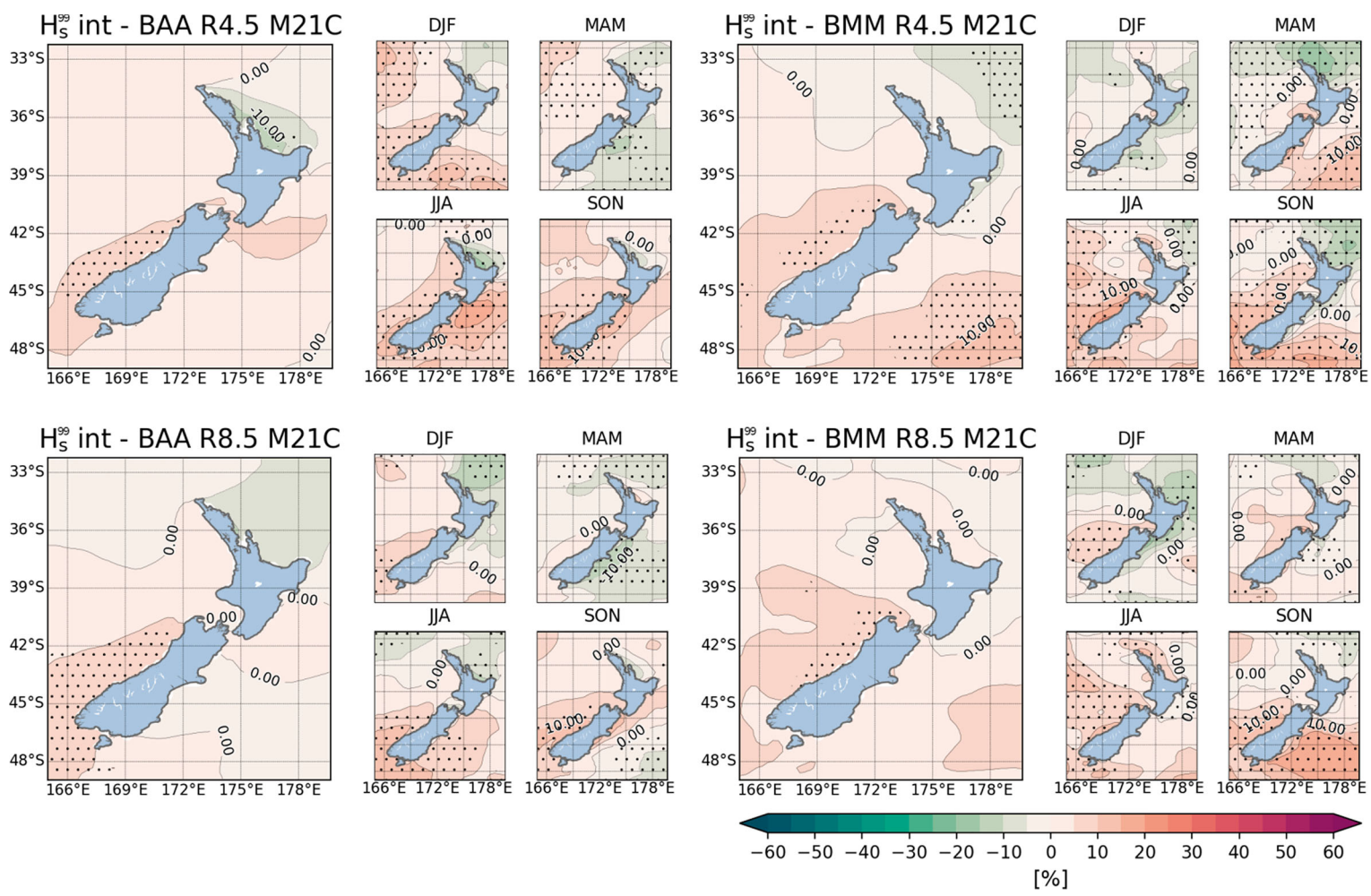


Figure 9. Annual (large panel) and seasonal (small panels) normalised H_s^{99} bias between the historic and projected (MID21C) periods of the ACCESS1.0 (right plots) and MIROC-5 (left plots) models, for RCPs 4.5 (top plots) and 8.5 (bottom plots). Austral summer, autumn, winter and spring are indicated by DJF, MAM, JJA and SON respectively. Bottom left colorbar indicates the normalised bias values between the time slices and the dots mark areas where changes are statistically significant.

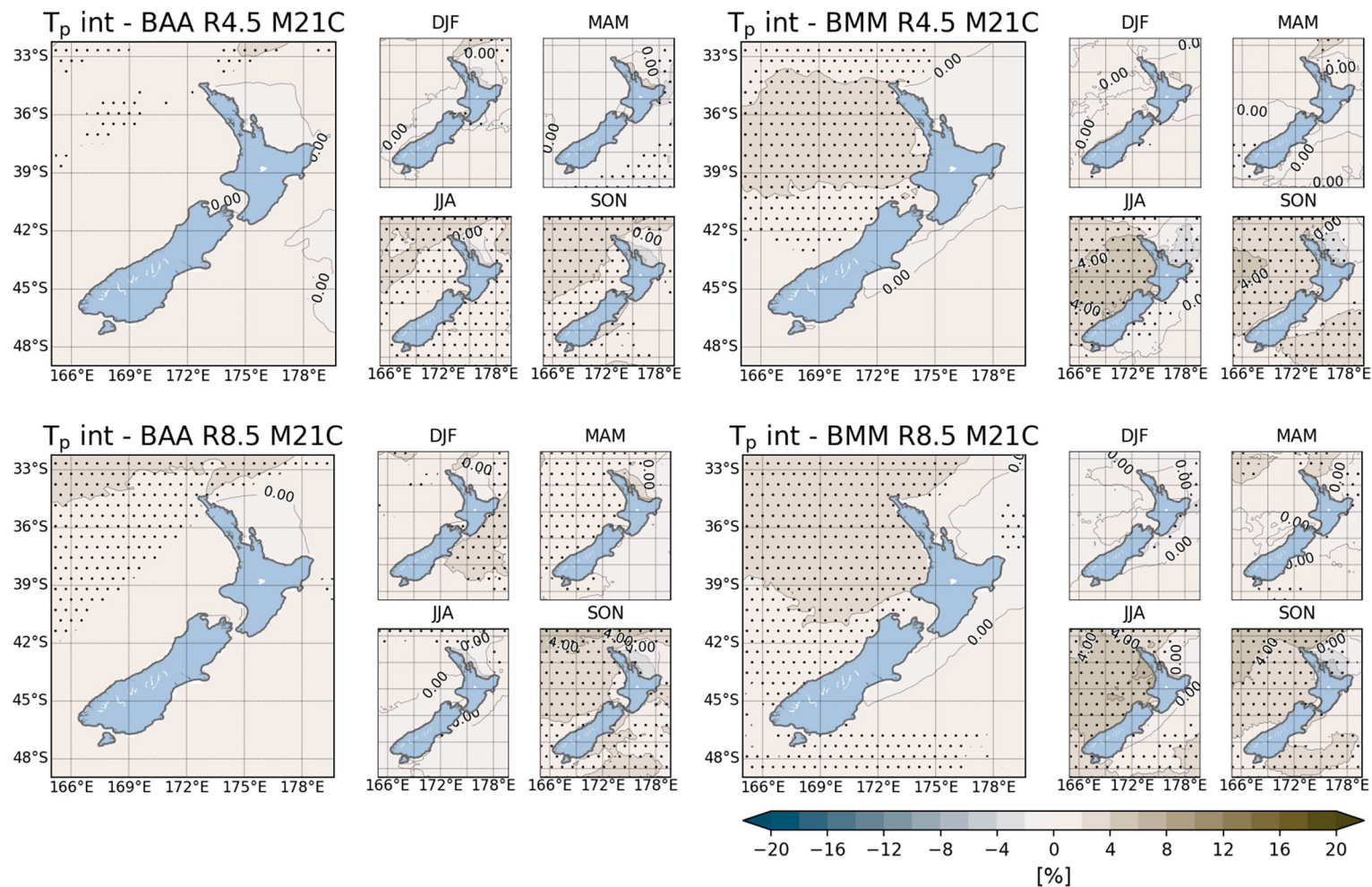


Figure 10. Annual (large panel) and seasonal (small panels) normalised T_p bias between the historic and projected (MID21C) periods of the ACCESS1.0 (right plots) and MIROC-5 (left plots) models, for RCPs 4.5 (top plots) and 8.5 (bottom plots). Austral summer, autumn, winter and spring are indicated by DJF, MAM, JJA and SON respectively. Bottom left colorbar indicates the normalised bias values between the time slices and the dots mark areas where changes are statistically significant.

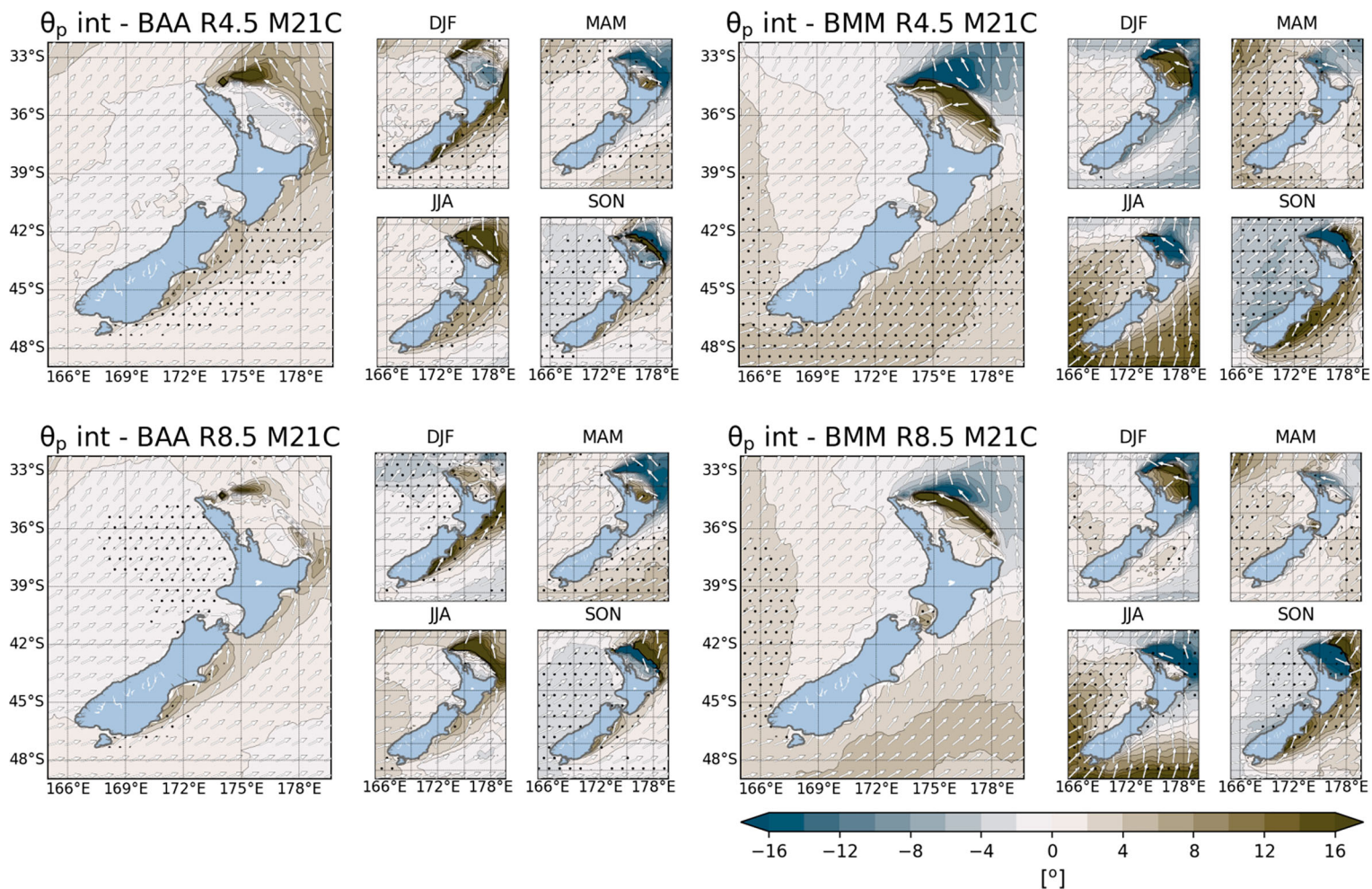


Figure 11. Annual (large panel) and seasonal (small panels) θ_p bias between the historic and projected (MID21C) periods of the ACCESS1.0 (right plots) and MIROC-5 (left plots) models, for RCPs 4.5 (top plots) and 8.5 (bottom plots). Austral summer, autumn, winter and spring are indicated by DJF, MAM, JJA and SON respectively. Bottom left colorbar indicates the directional bias values between the time slices and the dots mark areas where changes are statistically significant.

MIROC-5 (right plots of [Figure 10](#)), as well as the areas of significant changes. Annual means also show larger projected changes for RCP8.5 ([Figure 10](#), top plots) than for RCP4.5 ([Figure 10](#), bottom plots), for both ACCESS1.0 and MIROC-5. Seasonal plots of the ACCESS1.0 model show the largest areas of significant changes, as well as the largest values (from -2% to $>4\%$), in winter for RCP4.5 and spring for RCP8.5. For MIROC-5, the seasons with the largest extent of significant changes are winter and spring, with values ranging around $\pm 4\%$ in RCP4.5 and from -4% to 6% in RCP8.5.

Projected change of annual wave direction ([Figure 11](#)) is generally anti-clockwise along the west ($\sim -2^\circ$), and clockwise along the east coasts for both models (about 6° for ACCESS1.0, and 2° to 4° for MIROC-5, left and right plots of [Figure 11](#) respectively) and RCPs ([Figure 11](#), top plots for RCP4.5, bottom plots for RCP8.5). Along the west coast, models only disagree in the projected seasonal change in summer, for RCP8.5, with areas of significant change varying according to model and RCP. Along the east coast, the models show opposing changing patterns during summer for RCP4.5: through northeast, ACCESS1.0 anti-clockwise and MIROC-5 clockwise whilst ACCESS1.0 is clockwise and MIROC-5 is anti-clockwise along the southeast coast. Diverging patterns of projected seasonal change (positive for ACCESS1.0, negative for MIROC-5) are also present along the northeast coast during winter.

3.3. END21C projections

Projected changes for the END21C time slice (2081–2100), RCPs 4.5 and 8.5 are displayed in [Figures 12 to 15](#) for both the ACCESS1.0 and MIROC-5 models. Projected changes in mean annual H_s (large plots of [Figure 12](#)) are positive through the west coast and negative along most of the east coasts, with a larger area of positive change (values of up to $>10\%$) in RCP4.5 ([Figure 12](#), top) than in RCP8.5 ([Figure 12](#), bottom), and a larger negative projected change in RCP8.5 ($\sim 10\%$ for ACCESS1.0, $\sim 20\%$ for MIROC-5) than in RCP4.5 ($\sim 5\%$ for ACCESS1.0, $\sim 20\%$ for MIROC-5). The areas of statistically significant changes are present in both the regions of negative and positive changes, and are larger for ACCESS1.0 in RCP4.5 than in RCP8.5, whereas for MIROC-5 they are very similar in both RCPs. Seasonal data shows models agreeing well in sign on winter and spring (except for the south east coast during spring) for both RCPs, also with a large extent of statistically significant changes, whilst autumn shows the smallest agreement in sign between RCPs for both models.

Projected changes for events of extreme wave height of the ACCESS1.0 model (left of [Figure 13](#)) show a larger area of negative values for RCP4.5 ([Figure 13](#), top plots) than for RCP8.5 ([Figure 13](#), bottom plots) whereas MIROC-5 ([Figure 13](#), right) shows the opposite. The general spatial pattern still suggests an increase in wave height through the southwest, whilst along most of the other coasts the wave height is expected to decrease. Seasonal plots of both models and RCPs agree in a reduction of H_s^{99} during summer, and an increase (decrease) along the west (northeast) during winter and spring, yet with a few spatial differences between the areas of agreement in sign, depending on model and RCP. The extent of the statistically significant areas observed for H_s^{99} are larger for the END21C time slice than for the NEA21C time slice.

While for ACCESS1.0 model the projected change in annual mean T_p shows an overall decrease (down to -4%) along the northeast coast and an increase (up to 4%) throughout the west and southeast coasts ([Figure 14](#), left), for MIROC-5 we see a slight increase

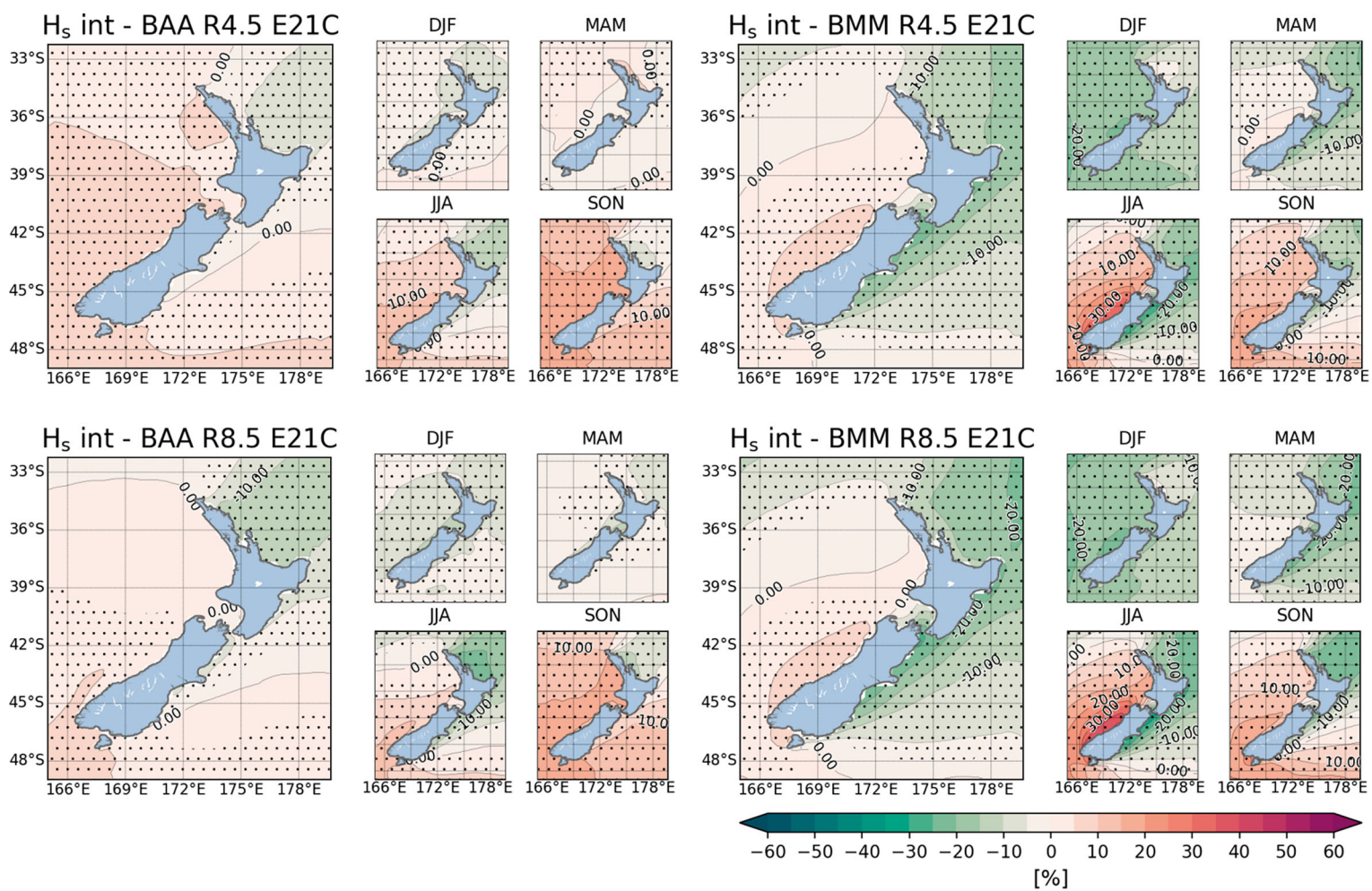


Figure 12. Annual (large panel) and seasonal (small panels) normalised H_s bias between the historic and projected (NEA21C) periods of the ACCESS1.0 (right plots) and MIROC-5 (left plots) models, for RCPs 4.5 (top plots) and 8.5 (bottom plots). Austral summer, autumn, winter and spring are indicated by DJF, MAM, JJA and SON respectively. Bottom left colorbar indicates the normalised bias values between the time slices and the dots mark areas where changes are statistically significant.

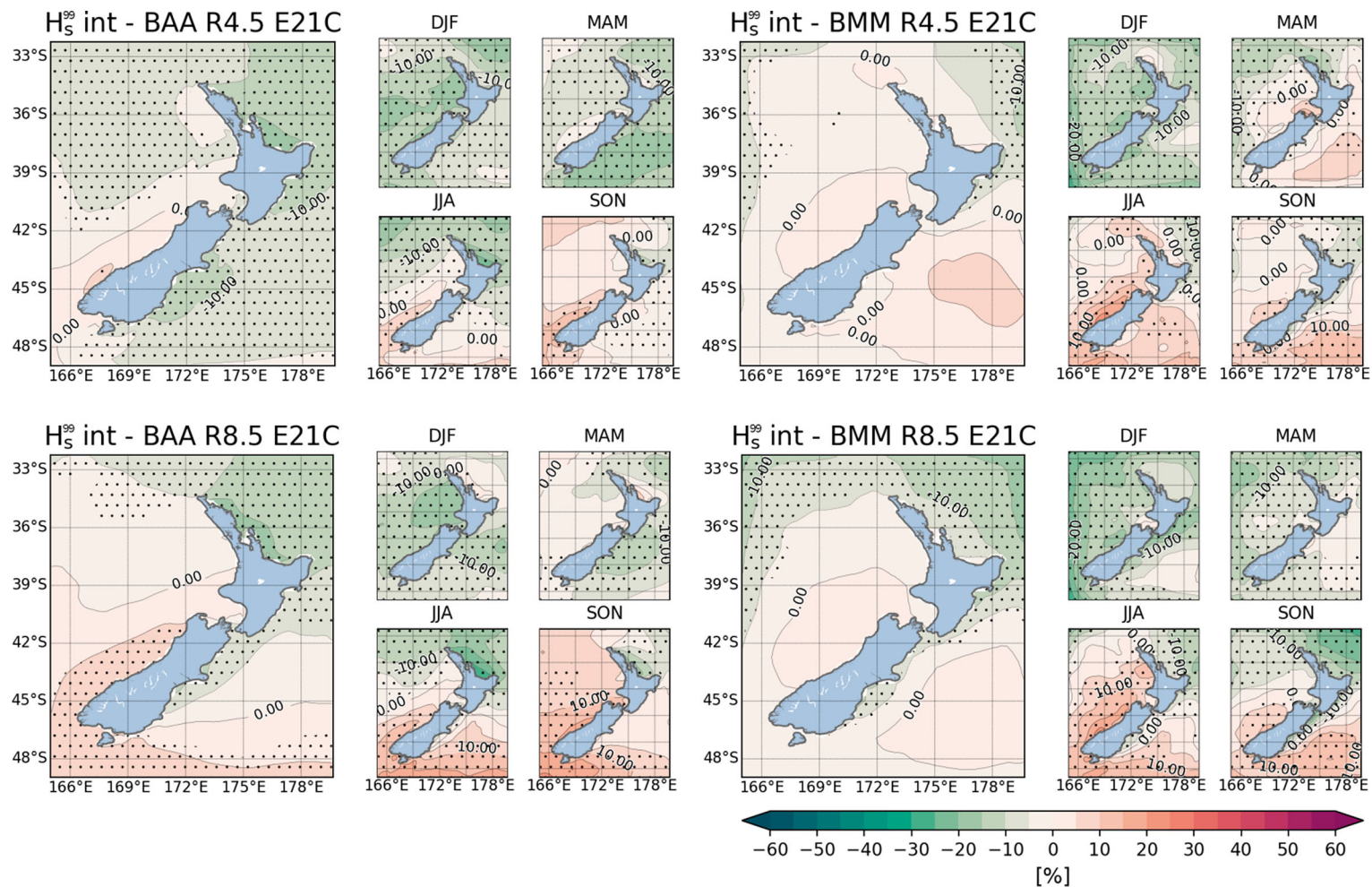


Figure 13. Annual (large panel) and seasonal (small panels) normalised H_s^{99} bias between the historic and projected (NEA21C) periods of the ACCESS1.0 (right plots) and MIROC-5 (left plots) models, for RCPs 4.5 (top plots) and 8.5 (bottom plots). Austral summer, autumn, winter and spring are indicated by DJF, MAM, JJA and SON respectively. Bottom left colorbar indicates the normalised bias values between the time slices and the dots mark areas where changes are statistically significant.

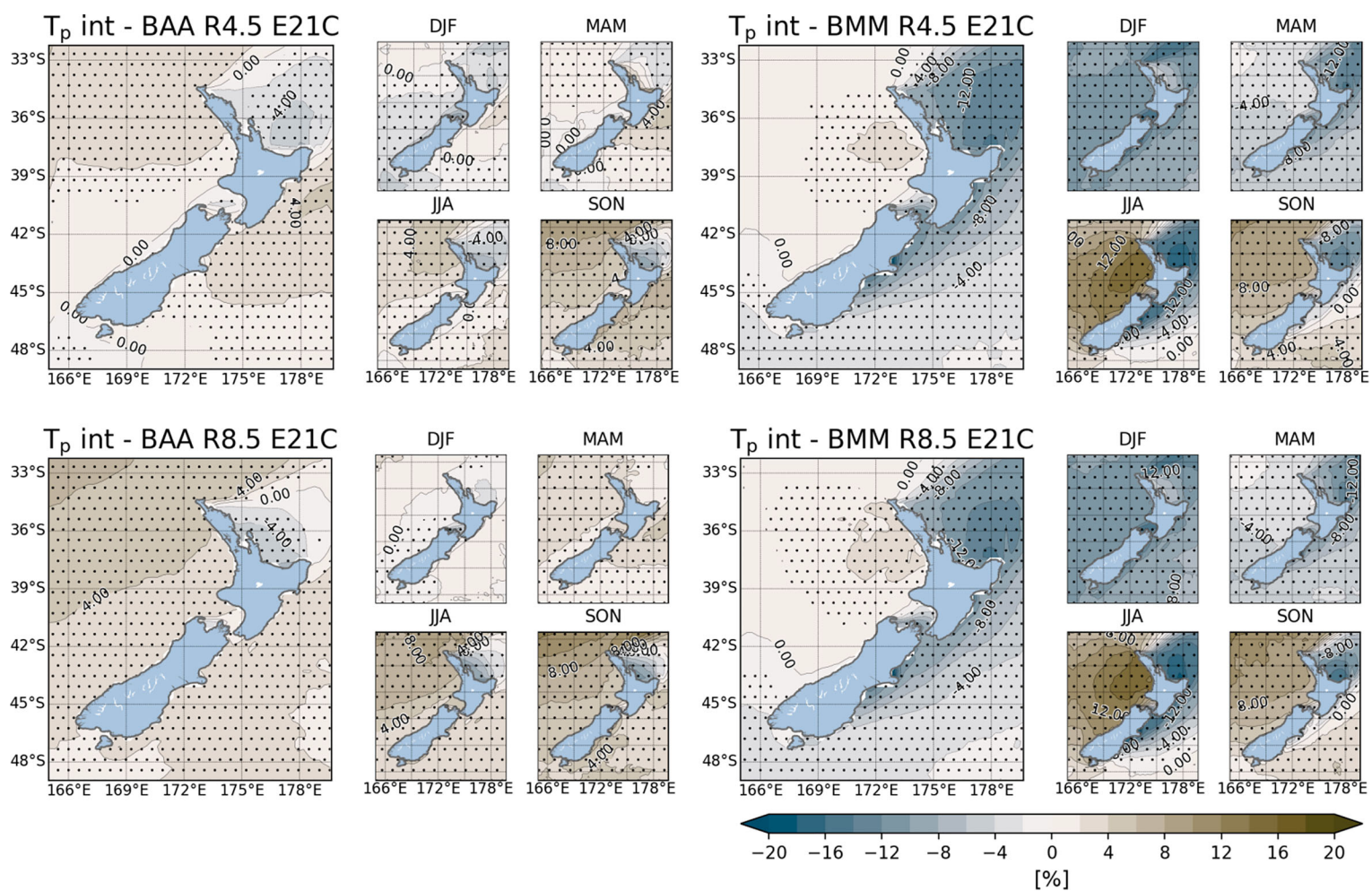


Figure 14. Annual (large panel) and seasonal (small panels) normalised T_p bias between the historic and projected (NEA21C) periods of the ACCESS1.0 (right plots) and MIROC-5 (left plots) models, for RCPs 4.5 (top plots) and 8.5 (bottom plots). Austral summer, autumn, winter and spring are indicated by DJF, MAM, JJA and SON respectively. Bottom left colorbar indicates the normalised bias values between the time slices and the dots mark areas where changes are statistically significant.

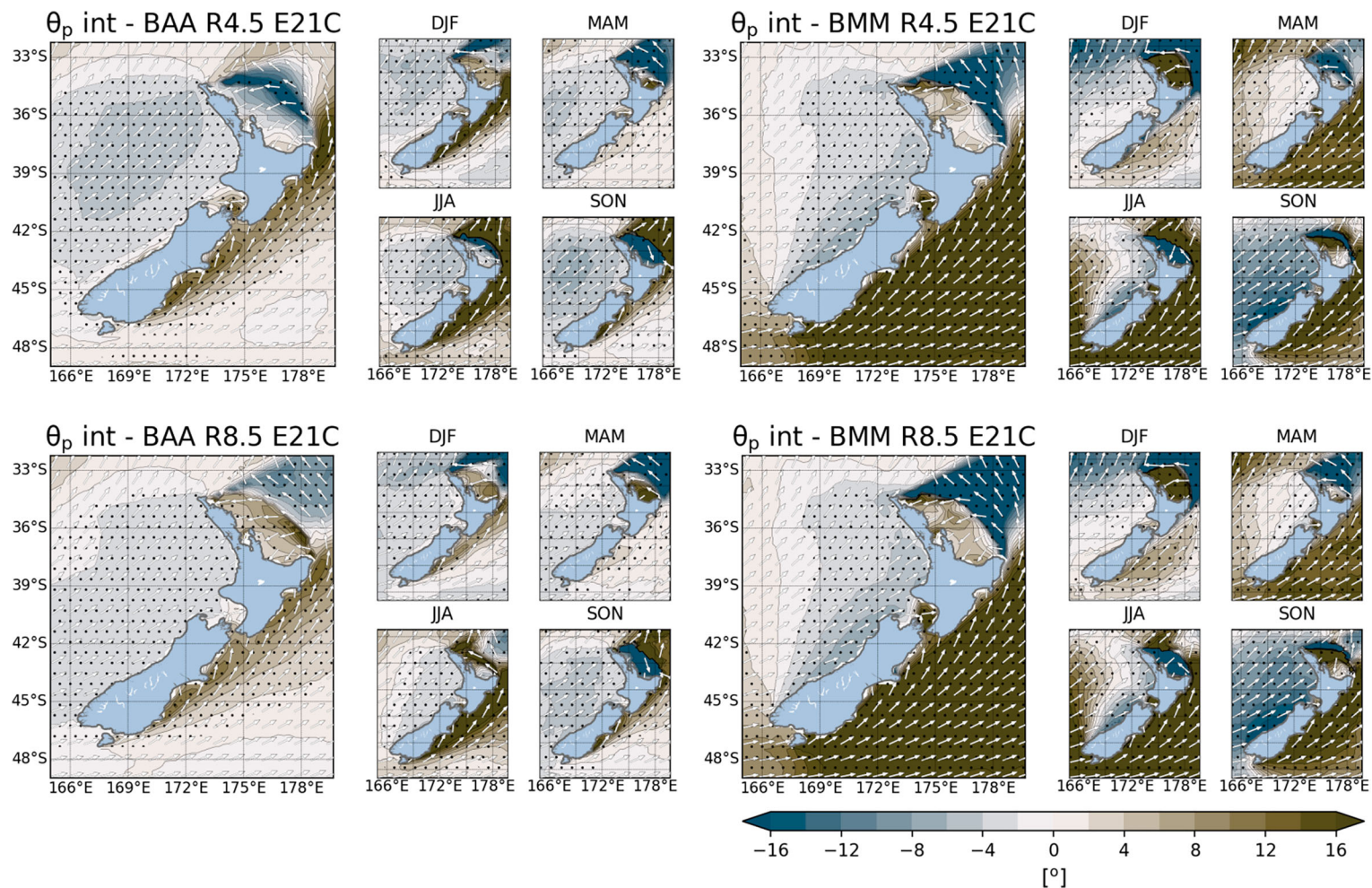


Figure 15. Annual (large panel) and seasonal (small panels) normalised θ_p bias between the historic and projected (NEA21C) periods of the ACCESS1.0 (right plots) and MIROC-5 (left plots) models, for RCPs 4.5 (top plots) and 8.5 (bottom plots). Austral summer, autumn, winter and spring are indicated by DJF, MAM, JJA and SON respectively. Bottom left colorbar indicates the directional bias values between the time slices and the dots mark areas where changes are statistically significant.

($\sim 2\%$) along the west and a substantial decrease (down to -12%) along the eastern coasts (Figure 14, right). The projected changes of ACCESS1.0 and MIROC-5 increase from RCP4.5 to RCP8.5 (top vs bottom plots of Figure 14), however, the difference between RCPs is subtle for MIROC-5. Statistical significance of the projected values is present where $|\text{pmbel}| > \sim 2\%$. Seasonal means show the largest increase in T_p for ACCESS1.0 during spring, followed by winter, and the opposite (largest increase in winter followed by spring) for MIROC-5. The largest decrease in T_p occurs in summer for both models, yet areas of increase are observed for ACCESS1.0.

Annual mean of peak wave direction projected change is anti-clockwise along the west coast and clockwise along the southeast coast for both models (Figure 15, left plots for ACCESS1.0, right plots for CNRM-CM5). Along the northeast coast, the statistical significance of the changes is mostly offshore – the change is partially anti-clockwise and clockwise for ACCESS1.0 in RCP4.5 (top plots of Figure 15), whereas for RCP8.5 (bottom plots of Figure 15) and CNRM-CM5 it is clockwise. Larger directional change is projected for ACCESS1.0 in RCP4.5 (2° to 6° along the west, 8° to 16° along the east) than in RCP8.5 (4° for the west, 6° to 12° for the east), while for CNRM-CM5, larger changes are expected along the west (4° to 8°) and east ($>16^\circ$) coasts for both RCPs. Seasonal values show the same directional pattern along the west and southeast coasts, with different intensities (and statistical significance) depending on model and RCP. For the northeast coast, the seasonal projected change is similar between ACCESS1.0 and CNRM-CM5 during summer (clockwise) and fall (anti-clockwise/clockwise), and the opposite during winter and spring.

3.4. Site-specific wave projections' summary and return period analysis

Essentially, we observe increasing wave heights along the south/west coast and decreasing wave heights along the north/east coast for annual mean values of H_s , with the intensity of the change increasing towards the end of the century. In general, the differences in mean H_s between the RCP scenarios are small ($< 5\%$), with RCP4.5 showing the largest positive change and RCP8.5 the largest negative change at the END21C period for both models. For H_s^{99} events, the extent of the observed positive change is larger in the NEA21C period, for both models and RCPs. Towards the END21C period, ACCESS1.0 shows larger values of positive change along the southwest, together with larger values of negative change along the north and southeast for RCP8.5, while an overall negative change is observed for RCP4.5. For MIROC-5, the projected change in H_s^{99} follows the same pattern observed in H_s during END21C: a larger positive change on RCP4.5 and a larger negative change on RCP8.5.

For wave period, the same trend of increasing (positive along the west, negative along the east) values towards the end of the century is observed. We note the increasing trend is similar between ACCESS1.0 and MIROC-5, with the latter showing the T_p increment over a larger area during the NEA21C, for the two RCPs. The increasing trend becomes more evident for ACCESS1.0 on RCP8.5 during the END21C time slice, whereas for MIROC-5, the most remarkable change is the reduction of T_p along the west coasts for the same RCP and time slice.

Projected wave direction of both models shows a progressive anti-clockwise rotation along the west and clockwise rotation along the southeast coast towards the end of the

Table 4. Summary table of projected changes for New Zealand at specific locations (Figure 2).

	w				n				e				s			
	H_s	H_s^{99}	T_p	θ_p	H_s	H_s^{99}	T_p	θ_p	H_s	H_s^{99}	T_p	θ_p	H_s	H_s^{99}	T_p	θ_p
AM4	3.2	4.6	0.3	0.1	-2.7	-10.6	-1.2	-1.9	-0.0	3.5	0.7	4.8	3.6	5.6	0.2	0.4
AM8	2.2	5.7	0.7	-0.7	-4.3	-7.5	-1.0	-0.1	-0.6	-0.6	0.7	4.6	3.4	6.5	0.6	0.4
AE4	6.0	0.5	0.6	-2.9	-6.3	-16.2	-4.3	1.0	-0.3	-10.0	2.3	11.5	8.5	0.0	-0.3	-1.3
AE8	3.6	5.2	2.6	-2.8	-11.8	-14.8	-4.8	4.1	-2.6	-6.4	2.6	9.9	6.3	8.1	1.8	-1.2
MM4	2.9	6.8	1.6	-0.3	-3.2	-2.6	-1.0	2.2	-2.1	2.6	-0.2	4.1	2.6	5.3	1.0	3.6
MM8	5.6	7.3	1.9	-0.0	1.0	2.1	-0.1	1.5	0.3	2.8	-0.3	2.3	3.7	5.0	1.4	2.5
ME4	5.9	2.7	1.1	-5.9	-13.3	-2.3	-12.3	2.0	-15.6	3.6	-8.5	20.8	5.1	-2.3	-1.5	7.6
ME8	5.5	2.2	1.0	-6.3	-16.0	-7.8	-12.4	5.0	-16.9	-3.0	-7.9	22.6	5.9	-2.6	-1.8	8.1

Note: The different wave parameters for points w (171.195° E, 41.021° S), n (176.809° E, 37.083° S), e (174.002° E, 43.552° S) and s (166.985° E, 46.927° S) are shown in columns. Rows show the models (A for ACCESS-1.0, M for MIROC5) under different scenarios (4 for RCP4.5, 8 for RCP8.5) and time slices (M for NEA21C, E for END21C). Bold values indicate statistically significant changes in seasonal means, bold italic values indicate statistically significant changes in annual means. Projected changes in H_s , H_s^{99} and T_p are shown in % while for θ_p are in and degrees.

century for the two RCPs. Along the northeast, the rotation is mostly clockwise for the two models, time slices and RCPs, except for ACCESS1.0, which shows anti-clockwise changes in RCP4.5 during the NEA21C and END21C time slices.

The results presented are quantified in Table 4, which shows projected changes at four different locations along the west (w), north (n), east (e) and south (s) of New Zealand. The sign and intensity of the changes vary for each point, time frame and RCP scenario. Despite the overall agreement between the models, point e shows some remarkable disagreement in wave height and wave period. It should be noted too that, despite the small number of parameters with statistically significant changes (annual mean) at each location, seasonally, nearly all the changes in parameters are statistically significant at these sites.

The POT method applied to the historic simulations identified an average of ~4 to ~5 storm events per year at the study sites for ACCESS1.0 and ~5 to ~8 for MIROC-5. The number of storm events identified during the projected simulations varied for each site according to time slice and RCP. Return periods of extreme events at each site show lower return levels for ACCESS1.0 (Figure 16) than for MIROC-5 (Figure 17). For ACCESS1.0, at site w, the return levels of wave height are larger for three out of the four projected periods, being NEA21C RCP8.5 and END21C RCP4.5 the time slices with the largest and lowest return levels respectively.

At points n and e, the historic return levels are higher than the projected levels, except for NEA21C RCP4.5 at site e. The lowest return levels are END21C RCP4.5 for point n and END21C RCP8.5 at point e. Finally, at site s the return levels are the largest (~9 to ~11 metres as opposed to ~6 to ~8 at the other sites) and show a relationship between return levels similar to site w, but with the largest return values expected for END21C RCP8.5 projection.

For MIROC-5, the return levels are larger for the projected time slices than for the historic simulation at points n and e, whereas at point w the historic return levels are below the NEA21C projections and above the END21C projections. At point s, the historic return levels are the largest, together with the NEA21C RCP8.5 period, which also shows the largest return levels at points w and n. At site e, the END21C RCP4.5 projection has the largest return levels.

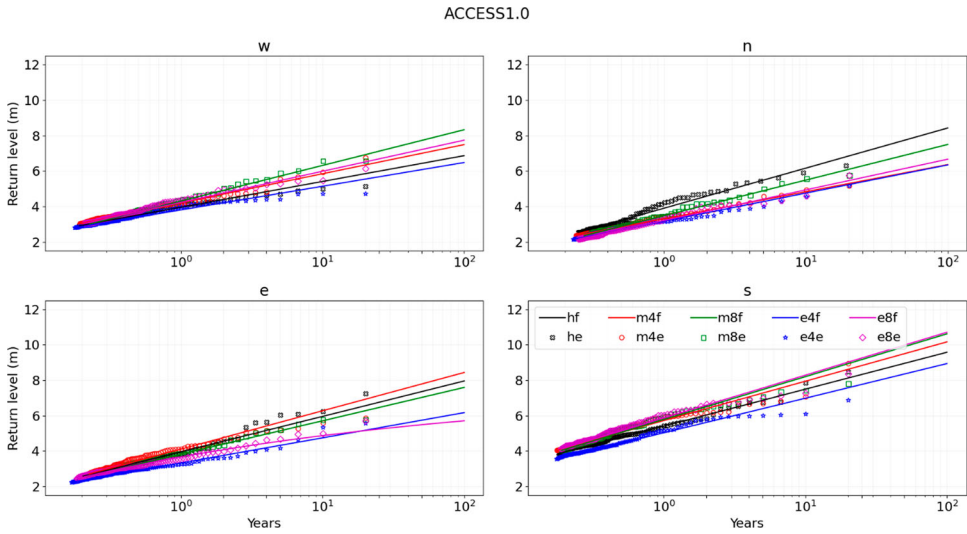


Figure 16. ACCESS1.0 historic and projected return periods of annual maxima at locations w (171.195° E, 41.021° S), n (176.809° E, 37.083° S), e (174.002° E, 43.552° S) and s (166.985° E, 46.927° S). Vertical and horizontal axes show the return levels and years, respectively. Lines represent values from the fitted GEV distribution, scatters show the GCM values.

4. Discussion

The methodology chosen to select the GCM has been successfully applied in a number of studies (Perez et al. 2014, 2015; Cagigal et al. 2020) and has ranked as first a model (ACCESS1.0) that can fairly represent the wave climate of New Zealand. However, our

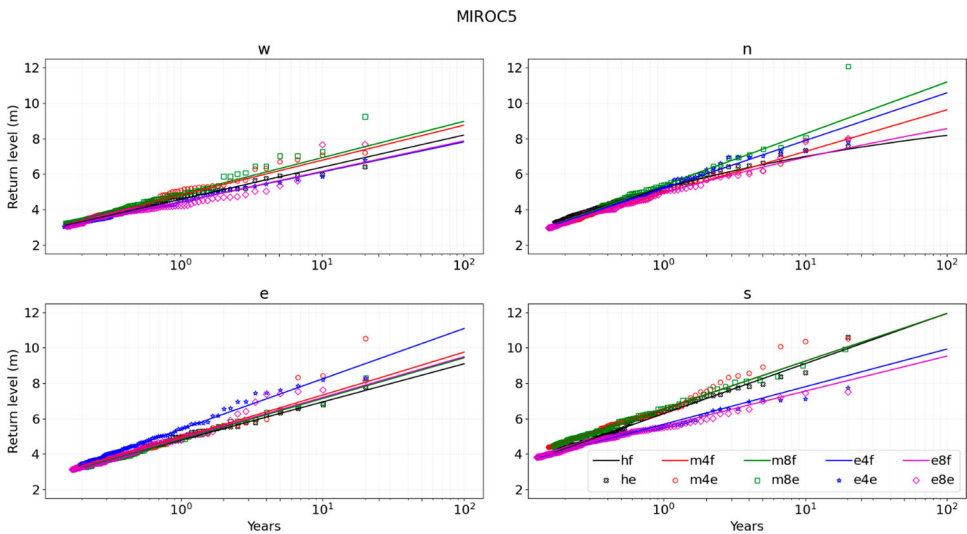


Figure 17. MIROC-5 historic and projected return periods of annual maxima at locations w (171.195° E, 41.021° S), n (176.809° E, 37.083° S), e (174.002° E, 43.552° S) and s (166.985° E, 46.927° S). Vertical and horizontal axes show the return levels and years, respectively. Lines represent values from the fitted GEV distribution, scatters show the GCM values.

analysis showed that MIROC5 (ranked as 4th) has better skill in representing wave height and period, in particular the H_s cumulative distribution. The 5th model in the rank (CNRM-CM5) did not perform as well as the others in terms of wave height and period, but was more skilled than MIROC-5 in representing the wave direction. The differences observed between the rank and the models' results can be attributed to the fact that the good skill of these GCM in simulating 'standard' climate variables (i.e. temperature, precipitation, etc.), does not imply the similar performance of such models for wave simulations (Hemer and Trenham 2016). At the same time, MIROC-5 and CNRM-CM5's unexpected skill in representing wave direction suggests a future investigation into how their weather patterns (SLP) frequency may influence wave height and direction.

The overall yearly and seasonal agreement between the 20yhcast, ACCESS1.0 and MIROC-5 suggests these models have good skill in simulating the wave climate around New Zealand. The differences observed in wave direction for the three models appear to be in line with the biases present in their wind directions (Figure 1 of the supplementary material). In general, the directional bias of the westerly winds across New Zealand could be explained by the models' coarse resolution and the complex orography of the North and South islands (Cavaleri and Bertotti 2004). As a result, an anti-clockwise shift in wave direction (comparable to the wind direction bias) observed eastwards of the Cook Strait is likely to be caused by the rough representation of the strait in the models and the under estimation of the wind channelling effects (Harris 1990; Albuquerque et al. 2021) associated to it. Other directional disparities in winds (e.g. clockwise northwards of 36° S and other seasonal biases in the westerlies) may be explained by the models' representation of the sub-tropical high and the trade winds, as well as the models' westerly jet location and bias. Clockwise wave direction bias along the arch off the northeast coast is likely to be caused by the biases in wind speed off this shore. The larger wind speed observed in the models generates more waves off this coast as the fetch distance increases, causing this change in wave direction. Another particular case worth noting is the anti-clockwise wave direction bias of MIROC-5 along the southeast of the domain, which is not in line with the wind direction bias. Such alteration is likely to be present in the swell waves and might be related to the characteristics of the model's westerly jet. In order to separate and quantify the amount of bias caused by the coarse winds from the directional bias present in the boundary forcings, two future studies are suggested: the first assessing the differences between wind-seas and swells for GCMs and the 20yhcast, and the second, conducting the downscaling of the GCMs forced waves using downscaled GCMs winds.

For biases in wave height and period, however, the potential causes are not as straightforward to define. The differences between GCMs and CFSR wind speed observed in our grid are able to explain part of the biases in H_s or T_p , for instance, the positive wind speed annual bias off the northeast coast, and the smaller annual bias of H_s and T_p along the same area. Regarding the remaining biases in H_s or T_p , which are present on the boundary forcings of our grids, they are likely to be related to the location and intensity of each GCM's westerly jet ($\sim 1.5^\circ$ northwards and ~ -1.7 m/s for ACCESS1.0, $\sim 2.8^\circ$ northwards and ~ -3.5 m/s for MIROC-5 and $\sim 2.7^\circ$ northwards and ~ -2.5 m/s for CNRM-CM5, as per Bracegirdle et al. (2013)), as well as other intrinsic model characteristics or limitations that are out of the scope of the present study.

With regard to wave climate projections, our results from ACCESS1.0 and MIROC-5 are in agreement with studies of global wave simulation ensembles for both CMIP3 and CMIP5 experiments (Hemer et al. 2013; Morim et al. 2019, among others). The wave climate changes projected to occur towards the twenty-first century are widely available in the literature and strongly tied to well-documented large-scale changes in atmospheric circulation patterns due to climate change. Along the Southern Ocean (and New Zealand area), the potential main drivers for projected changes are the poleward shift and intensification of the westerly jet (Barnes and Polvani 2013; Bracegirdle et al. 2017), as well as the same directional shift of the high-pressure sub-tropical ridge (Hemer et al. 2013) and the extra-tropical storm tracks (Bengtsson et al. 2006; Shaw et al. 2016).

The westerly jet shift and intensification can cause a general increase in H_s and T_p , as well as a counter-clockwise rotation of θ_p along the areas exposed to these waves (Hemer et al. 2013). Such changes have been observed in our results, with different intensities for each model, time slice and RCP scenario.

Low wind speeds are associated with the latitudes adjacent to the sub-tropical high ridge. Southwards of the ridge, the westerlies reduce in speed and the extra-tropical storms are blocked (Hemer et al. 2013; Wandres et al. 2017), which can induce a decrease in wave height along New Zealand's north and east coasts as the sub-tropical high shifts southwards. Such displacement of the sub-tropical high can be observed by the change in signal of the yearly wind bias, and by the shift of this change of signal northwards during austral winter and spring, and southwards during summer and autumn (supplementary Figures 2 and 3).

For ACCESS1.0 and MIROC-5, the projected changes in mean wave height for RCP8.5 are smaller than for RCP4.5 on the END21C time slice. However, the projected changes in wave period and wave direction are larger. This can be explained by the stronger poleward shift of the westerly jet by the end of the twenty-first century in RCP8.5, and a degradation of the waves generated in the Southern Ocean into swells before reaching New Zealand. Such swells are likely to contribute less with the wave height than with the wave period and direction. A future study analysing swells and wind-seas separately is suggested, as this data was also produced in our simulations.

For extreme wave heights, the positive changes along the west and south coasts (represented by points w and s) we see in ACCESS1.0 during the NEA21C period can be related to the increased intensity of storms on this time slice for both RCPs (see Table 1 of the supplementary material). For the END21C period, while the intensification of the storms can explain the projected increase in wave height observed on RCP8.5, the larger number of storms with smaller intensity in RCP4.5 appears to cause the projected increase in H_s^{99} . Along the area represented by point n, the decrease in extreme wave height events may be due to the decrease in the intensity of the storms. The east coast (represented by point e) shows an increase in H_s^{99} (for NEA21C and RCP4.5) which may be caused by the reduced number of more intense storms, and a decrease in H_s^{99} , potentially caused by a larger number of extreme events of lower intensity. The same relationship between the projected increase in H_s^{99} and the number/intensity of storms shown for ACCESS1.0 is likely to drive the projected changes and return periods for MIROC-5, as per supplementary Table 1.

Many of the studies on wave projections rely on ensembles of models which, provide benefits such as (i) reduced biases during historical simulations, as models whose results

are too far from the other ensemble members are likely to be outweighed on the ensemble mean, (ii) the identification of areas of robust projected changes, based on the agreement of the ensemble members and (iii) the possibility of isolating and quantifying the uncertainties within each model simulation.

Despite the value of the wave ensemble-based studies, the benefits of individual model analysis are also evident. New Zealand lies in an area where the wave and atmospheric changes are quite sensitive to the scenarios and time slices, as it is widely exposed to the large atmospheric processes that are being altered by climate change (i.e. shifts of the sub-tropical high, westerly jet and storm tracks), and differently affected by each of them. Along this area, where every model has a specific bias, the annual and seasonal displacements of the sub-tropical high are likely to be smoothed out by the ensemble mean, which can potentially hinder the identification of such displacements, in particular for NEA21C projections.

Within the scenarios and time slices considered for the present study, the spatial distribution of the changes in projected wave height of the ACCESS1.0 and MIROC-5 models also follows the variability in the position and width of the sub-tropical high ridge. The model with the largest shift of the ridge (i.e. MIROC-5) projects the largest negative change along the eastern coasts – such patterns are evident for both the annual and seasonal mean biases observed along the northeast and east coasts. The projected intensification of the trade winds, which has been documented in the literature, is not as clear to observe due to the size of our domain. Along the west, the projected changes can be related to the shifts of the westerly jet and the storm tracks, which become more evident during winter and autumn – yet the predominant pattern is a projected increase in wave height and wind speed, the reader should note that for both models there are changes in the number and intensity of extreme events.

We must stress to the reader at this point that our study is based on the assumption that the bias between the models and the 20yhcast remains the same during the historical and projected periods. Even though the same approach has been adopted in other studies in the literature (Lemos et al. 2020), we recommend our results be interpreted qualitatively, and with a relative sense to the wave climate of the area.

The projected changes affect sediment transport, coastal mixing and erosion, as these processes are dependent on the incident energy flux (Masselink and Pattiaratchi 2001; Wandres et al. 2017). Since shoreline stability is sensitive to directional wave changes (Harley et al. 2017; Barnard et al. 2017), the projected anomalies can severely affect the current equilibrium state of New Zealand's beaches as well as nearshore structures. Hence, the database here presented can be of great value for studies of the assessment and mitigation of coastal hazards driven by climate change.

5. Conclusion

The present study simulated the nearshore projected changes in the wave climate of New Zealand using three models of the 5th phase of the Climate Model Intercomparison Project: ACCESS1.0, MIROC5 and CNRM-CM5. The simulations included the historic (1986–2005), near-term (2026–2045) and end (2081–2100) of the

twenty-first-century time slices. The two projected periods were simulated under two different representative concentration pathways (RCP4.5 and RCP8.5). The models were chosen based on their skill in representing the weather patterns of New Zealand from reanalysis data during their historic experiments and the availability of boundary forcings with the same wave modelling method, which were obtained from the Coordinated Ocean Wave Climate Project. Bimodal spectral boundary forcings of models historic and projected periods were reconstructed using the JONSWAP formulation and a k-NN regressor to define values of directional spread. Waves of the historic and projected experiments were downscaled with the SWAN wave model. The models' skill in representing the regional wave climate was estimated by comparing their historic period with a 20-year hindcast of New Zealand. The two best-performing models in representing the historical regional wave climate of New Zealand had their projected changes assessed and our main findings are summarised below:

- The k-NN regressor is a good estimator for values of directional spread
- Wave height and period projected changes consist of an increase along the west/south and a decrease throughout the north/east coasts of New Zealand
- Projected wave directions show a counter-clockwise rotation along the west coast due to the southward shift and intensification of the westerly jet, and a clockwise rotation along the southwest
- Seasonality of projected changes is larger than the annual mean, and shows larger areas of statistically significant results compared to the annual means
- In RCP4.5, due to a smaller poleward shift of the westerly jet, the positive pmbe in mean wave height is larger than in RCP8.5 in the END21C time slice. The positive pmbe in T_p and θ_p however, are larger in RCP8.5
- Model agreement in terms of projected POT events suggests a reduction in the number of storms but an increase in storm intensity along the west and south coasts for NEA21C RCP8.5 (and the opposite for END21C RCP4.5), a reduction in the intensity of the storms along the north for END21C RCP8.5, an increase in the number of storms with a reduction on their intensity along the east for END21C RCP8.5
- The projected reduction in wave height along the northeast coast is likely to be caused by a poleward shift of the high-pressure sub-tropical ridge
- The analysis of individual model ensembles over a relatively wide range of RCP scenarios and time slices allows for a better identification and understanding of the wave/atmosphere changes projected to occur towards the end of the century. This is particularly interesting for New Zealand due to its position regarding the sub-tropical ridge and the westerly jet

Acknowledgments

All the programming code for this research was written in Python programming language (www.python.org) and all the plots displayed were created with python's matplotlib module (Hunter 2007). Finally, the authors wish to thank all the scientists that have contributed in building the databases used in the present study.

Disclosure statement

No potential conflict of interest was reported by the author(s).

Funding

The current research is funded by the now defunct GNS-MBIE research programme 'Climate impacts on weather-related hazards', through a grant to GC (contract 3710440). FJM acknowledges the Spanish Ministry of Science for the funding of project PID2019-107053RB-I00.

ORCID

João Albuquerque  <http://orcid.org/0000-0003-3686-4997>
Jose A. A. Antolínez  <http://orcid.org/0000-0002-0694-4817>
Fernando J. Méndez  <http://orcid.org/0000-0002-5005-1100>
Giovanni Coco  <http://orcid.org/0000-0001-7435-1602>

References

- Albuquerque J, Antolínez JA, Gorman RM, Méndez FJ, Coco G. 2021. Seas and swells throughout New Zealand: a new partitioned hindcast. *Ocean Modelling*. 168:101897. <https://doi.org/10.1016/j.ocemod.2021.101897>.
- Albuquerque J, Antolínez JAA, Rueda A, Méndez FJ, Coco G. 2018. Directional correction of modeled sea and swell wave heights using satellite altimeter data. *Ocean Modelling*. 131:103–114. <https://doi.org/10.1016/j.ocemod.2018.09.001>.
- Altman NS. 1992. An introduction to kernel and nearest-neighbor nonparametric regression. *The American Statistician*. 46:175–185. <https://doi.org/10.1080/00031305.1992.10475879>.
- Arblaster JM, Meehl GA, Karoly DJ. 2011. Future climate change in the southern hemisphere: competing effects of ozone and greenhouse gases. *Geophysical Research Letters*. 38(2). <https://doi.org/10.1029/2010GL045384>.
- Ardhuin F, Hanafin J, Quilfen Y, Chapron B, Queffeulou P, Obrebski M, Sienkiewicz J, Vandemark D. 2011. Calibration of the IOWAGA global wave hindcast (1991–2011) using ECMWF and CFSR winds. *Proceedings of the 12th International Workshop of Wave Hindcasting and Forecasting*. Hawaii.
- Ashok K, Nakamura H, Yamagata T. 2007. Impacts of ENSO and Indian Ocean dipole events on the southern hemisphere storm-track activity during austral winter. *Journal of Climate*. 20:3147–3163. <https://doi.org/10.1175/JCLI4155.1>.
- Barnard PL, Hoover D, Hubbard DM, Snyder A, Ludka BC, Allan J, Kaminsky GM, Ruggiero P, Gallien TW, Gabel L, et al. 2017. Extreme oceanographic forcing and coastal response due to the 2015–2016 El Niño. *Nature Communications*. 8:1–8.
- Barnes EA, Polvani L. 2013. Response of the midlatitude jets, and of their variability, to increased greenhouse gases in the CMIP5 models. *Journal of Climate*. 26:7117–7135. <https://doi.org/10.1175/JCLI-D-12-00536.1>.
- Bengtsson L, Hodges KI, Roeckner E. 2006. Storm tracks and climate change. *Journal of Climate*. 19:3518–3543. <https://doi.org/10.1175/JCLI3815.1>.
- Bidlot J-R, Janssen P, Abdalla S, Hersbach H. 2007. A revised formulation of ocean wave dissipation and its model impact; p. 27. <https://doi.org/10.21957/m97gmhqe>.
- Booij N, Ris RC, Holthuijsen LH. 1999. A third-generation wave model for coastal regions: 1. Model description and validation. *Journal of Geophysical Research Oceans*. 104:7649–7666.
- Bracegirdle TJ, Hyder P, Holmes CR. 2017. CMIP5 diversity in southern westerly jet projections related to historical sea ice area: strong link to strengthening and weak link to shift. *Journal of Climate*. 31:195–211. <https://doi.org/10.1175/JCLI-D-17-0320.1>.

- Bracegirdle TJ, Shuckburgh E, Saltee J -B, Wang Z, Meijers AJS, Bruneau N, Phillips T, Wilcox LJ. 2013. Assessment of surface winds over the Atlantic, Indian, and Pacific Ocean sectors of the southern ocean in CMIP5 models: historical bias, forcing response, and state dependence. *Journal of Geophysical Research Atmospheres*. 118:547–562. <https://doi.org/10.1002/jgrd.50153>.
- Bricheno LM, Wolf J. 2018. Future wave conditions of Europe, in response to high-end climate change scenarios. *Journal of Geophysical Research Oceans*. 123:8762–8791.
- Cagigal L, Rueda A, Castanedo S, Cid A, Perez J, Stephens SA, Coco G, Méndez FJ. 2020. Historical and future storm surge around New Zealand: from the 19th century to the end of the 21st century. *International Journal of Climatology*. 40:1512–1525. <https://doi.org/10.1002/joc.6283>.
- Camargo SJ, Wing AA. 2016. Tropical cyclones in climate models. *WIREs Climate Change*. 7:211–237. <https://doi.org/10.1002/wcc.373>.
- Camus P, Losada I, Izaguirre C, Espejo A, Menéndez M, Pérez J. 2017. Statistical wave climate projections for coastal impact assessments. *Earth's Future*. 5:918–933.
- Cavaleri L, Bertotti L. 2004. Accuracy of the modelled wind and wave fields in enclosed seas. *Tellus A: Dynamic Meteorology and Oceanography*. 56:167–175.
- Cavaleri L, Fox-Kemper B, Hemer M. 2012. Wind waves in the coupled climate system. *Bulletin of the American Meteorological Society*. 93:1651–1661.
- Chen WY. 1982. Assessment of southern oscillation sea-level pressure indices. *Monthly Weather Review*. 110:800–807. [https://doi.org/10.1175/1520-0493\(1982\)110<0800:AOSOSL>2.0.CO;2](https://doi.org/10.1175/1520-0493(1982)110<0800:AOSOSL>2.0.CO;2).
- Collins M, Knutti R, Arblaster J, Dufresne J-L, Fichefet T, Friedlingstein P, Gao X, Gutowski WJ, Johns T, Krinner G, et al. 2013. Long-term climate change: projections, commitments and irreversibility. In: *Climate change 2013 – the physical science basis: contribution of working group I to the fifth assessment report of the intergovernmental panel on climate change*. Cambridge University Press; p. 1029–1136.
- Couvelard X, Lemarié F, Samson G, Redelsperger J-L, Ardhuin F, Benshila R, Madec G. 2020. Development of a two-way-coupled ocean–wave model: assessment on a global nemo(v3.6)–ww3(v6.02) coupled configuration. *Geoscientific Model Development*. 13:3067–3090. <https://doi.org/10.5194/gmd-13-3067-2020>.
- Cox AT, Swail VR. 2001. A global wave hindcast over the period 1958–1997 – validation and climate assessment. *Journal of Geophysical Research Oceans*. 106:2313–2329.
- Dee DP, Uppala SM, Simmons AJ, Berrisford P, Poli P, Kobayashi S, Andrae U, Balmaseda MA, Balsamo G, Bauer P, et al. 2011. The era-interim reanalysis: configuration and performance of the data assimilation system. *Quarterly Journal of the Royal Meteorological Society*. 137:553–597. <https://doi.org/10.1002/qj.828>.
- Diamond H, Renwick J. 2015. The climatological relationship between tropical cyclones in the southwest Pacific and the southern annular mode. *International Journal of Climatology*. 35:613–623.
- Dobrynin M, Murawsky J, Yang S. 2012. Evolution of the global wind wave climate in CMIP5 experiments. *Geophysical Research Letters*. 39(18).
- Erikson LH, Hegermiller C, Barnard PL, Ruggiero P, van Ormondt M. 2015. Projected wave conditions in the eastern north Pacific under the influence of two CMIP5 climate scenarios. *Ocean Modelling*. 96:171–185.
- Ewans KC. 2001. Directional spreading in ocean swell. *Ocean Wave Measurement and Analysis*: 517–529.
- Favre A, Gershunov A. 2009. North Pacific cyclonic and anticyclonic transients in a global warming context: possible consequences for western north American daily precipitation and temperature extremes. *Climate Dynamics*. 32:969–987.
- Feng S, Hu Q, Huang W, Ho C-H, Li R, Tang Z. 2014. Projected climate regime shift under future global warming from multi-model, multi-scenario CMIP5 simulations. *Global Planetary Change*. 112:41–52. <https://doi.org/10.1016/j.gloplacha.2013.11.002>.
- Forristall GZ, Ewans KC. 1998. Worldwide measurements of directional wave spreading. *Journal of Atmospheric and Oceanic Technology*. 15:440–469. [https://doi.org/10.1175/1520-0426\(1998\)015<0440:WMODWS>2.0.CO;2](https://doi.org/10.1175/1520-0426(1998)015<0440:WMODWS>2.0.CO;2).

- Godoi VA, Bryan KR, Gorman RM. 2016. Regional influence of climate patterns on the wave climate of the southwestern Pacific: the New Zealand region. *Journal of Geophysical Research Oceans*. 121:4056–4076. <https://doi.org/10.1002/2015JC011572>.
- Gordon ND. 1986. The southern oscillation and New Zealand weather. *Monthly Weather Review*. 114:371–387.
- Gorman RM, Bryan KR, Laing AK. 2003a. Wave hindcast for the New Zealand region: deep-water wave climate. *New Zealand Journal of Marine and Freshwater Research*. 37:589–612.
- Gorman RM, Bryan KR, Laing AK. 2003b. Wave hindcast for the New Zealand region: nearshore validation and coastal wave climate. *New Zealand Journal of Marine and Freshwater Research*. 37:567–588.
- Griffiths G. 2011. Drivers of extreme daily rainfalls in New Zealand. *Weather Climate*. 31:24–49.
- Harley MD, Turner IL, Kinsela MA, Middleton JH, Mumford PJ, Splinter KD, Phillips MS, Simmonds JA, Hanslow DJ, Short AD. 2017. Extreme coastal erosion enhanced by anomalous extratropical storm wave direction. *Scientific Reports*. 7:1–9.
- Harris TFW. 1990. Greater Cook Strait: form and flow. *DSIR Marine and Freshwater*.
- Hasselmann K, Barnett T, Bouws E, Carlson H, Cartwright D, Enke K, Ewing J, Gienapp H, Hasselmann D, Kruseman P, et al. 1973. Measurements of wind-wave growth and swell decay during the Joint North Sea Wave Project (JONSWAP). *Ergänzungsheft 8-12*.
- Haver S, Nyhus KA. 1986. A wave climate description for long term response calculations. In: *Fifth International Symposium on Offshore Mechanics and Arctic Engineering*. Vol. 4. Tokyo; p. 27.
- Hemer MA, Fan Y, Mori N, Semedo A, Wang XL. 2013. Projected changes in wave climate from a multi-model ensemble. *Nature Climate Change*. 3:471–476.
- Hemer MA, Katzfey J, Trenham CE. 2013. Global dynamical projections of surface ocean wave climate for a future high greenhouse gas emission scenario. *Ocean Modelling*. 70:221–245.
- Hemer MA, McInnes KL, Ranasinghe R. 2013. Projections of climate change-driven variations in the offshore wave climate off south eastern Australia. *International Journal of Climatology*. 33:1615–1632. <https://doi.org/10.1002/joc.3537>.
- Hemer MA, Trenham CE. 2016. Evaluation of a CMIP5 derived dynamical global wind wave climate model ensemble. *Ocean Modelling*. 103:190–203.
- Hemer MA, Wang XL, Weisse R, Swail VR. 2012. Advancing wind-waves climate science: the COWCLIP project. *Bulletin of the American Meteorological Society*. 93:791–796. <https://doi.org/10.1175/BAMS-D-11-00184.1>.
- Hunter JD. 2007. Matplotlib: a 2D graphics environment. *Computing in Science & Engineering*. 9:90–95.
- Kidston J, Renwick JA, McGregor J. 2009. Hemispheric-scale seasonality of the southern annular mode and impacts on the climate of New Zealand. *Journal of Climate*. 22:4759–4770. <https://doi.org/10.1175/2009JCLI2640.1>.
- Lemos G, Menendez M, Semedo A, Camus P, Hemer M, Dobrynin M, Miranda PM. 2020. On the need of bias correction methods for wave climate projections. *Global Planetary Change*. 186:103109.
- Lionello P, Cogo S, Galati M, Sanna A. 2008. The Mediterranean surface wave climate inferred from future scenario simulations. *Global Planetary Change*. 63:152–162.
- Madden RA, Julian PR. 1971. Detection of a 40–50 day oscillation in the zonal wind in the tropical Pacific. *Journal of Atmospheric Sciences*. 28:702–708.
- Marshall AG, Hemer MA, Hendon HH, McInnes KL. 2018. Southern annular mode impacts on global ocean surface waves. *Ocean Modelling*. 129:58–74. <https://doi.org/10.1016/j.ocemod.2018.07.007>.
- Masselink G, Pattiaratchi C. 2001. Seasonal changes in beach morphology along the sheltered coastline of Perth, Western Australia. *Marine Geology*. 172:243–263. [https://doi.org/10.1016/S0025-3227\(00\)00128-6](https://doi.org/10.1016/S0025-3227(00)00128-6).
- Méndez FJ, Menéndez M, Luceño A, Losada IJ. 2006. Estimation of the long-term variability of extreme significant wave height using a time-dependent peak over threshold (pot) model. *Journal of Geophysical Research Oceans*. 111(C7).

- Mentaschi L, Vousedoukas MI, Voukouvalas E, Dosio A, Feyen L. 2017. Global changes of extreme coastal wave energy fluxes triggered by intensified teleconnection patterns. *Geophysical Research Letters*. 44:2416–2426.
- Meucci A, Young IR, Hemer M, Kirezci E, Ranasinghe R. 2020. Projected 21st century changes in extreme wind-wave events. *Science Advances*. 6:eaaz7295.
- Mitchell J, Mackay K, Neil H, Mackay E, Pallentin A, Notman P. 2012. Undersea New Zealand, 1:5, 000, 000. NIWA Chart, Miscellaneous Series. 92.
- Mori N, Yasuda T, Mase H, Tom T, Oku Y. 2010. Projection of extreme wave climate change under global warming. *Hydrological Research Letters*. 4:15–19.
- Morim J, Hemer M, Wang XL, Cartwright N, Trenham C, Semedo A, Young I, Brichenno L, Camus P, Casas-Prat M, et al. 2019. Robustness and uncertainties in global multivariate wind-wave climate projections. *Nature Climate Change*. 9:711–718.
- Moss RH, Edmonds JA, Hibbard KA, Manning MR, Rose SK, Van Vuuren DP, Carter TR, Emori S, Kainuma M, Kram T, et al. 2010. The next generation of scenarios for climate change research and assessment. *Nature*. 463:747–756.
- Perez J, Menendez M, Camus P, Mendez FJ, Losada IJ. 2015. Statistical multi-model climate projections of surface ocean waves in Europe. *Ocean Modelling*. 96:161–170.
- Perez J, Menendez M, Mendez FJ, Losada IJ. 2014. Evaluating the performance of CMIP3 and CMIP5 global climate models over the north-east Atlantic region. *Climate Dynamics*. 43:2663–2680.
- Rasclé N, Ardhuin F. 2013. A global wave parameter database for geophysical applications. Part 2: model validation with improved source term parameterization. *Ocean Modelling*. 70:174–188.
- Rasclé N, Ardhuin F, Queffelec P, Croizé-Fillon D. 2008. A global wave parameter database for geophysical applications. Part 1: wave-current-turbulence interaction parameters for the open ocean based on traditional parameterizations. *Ocean Modelling*. 25:154–171.
- Rivière G. 2011. A dynamical interpretation of the poleward shift of the jet streams in global warming scenarios. *Journal of Atmospheric Sciences*. 68:1253–1272.
- Rueda A, Cagigal L, Antolínez JAA, Albuquerque JC, Castanedo S, Coco G, Méndez FJ. 2019. Marine climate variability based on weather patterns for a complicated island setting: the New Zealand case. *International Journal of Climatology*. 39:1777–1786. <https://doi.org/10.1002/joc.5912>.
- Semedo A, Dobrynin M, Lemos G, Behrens A, Staneva J, De Vries H, Sterl A, Bidlot J-R, Miranda P, Murawski J. 2018. CMIP5-derived single-forcing, single-model, and single-scenario wind-wave climate ensemble: configuration and performance evaluation. *Journal of Marine Science and Engineering*. 6:90.
- Semedo A, Weisse R, Behrens A, Sterl A, Bengtsson L, Günther H. 2012. Projection of global wave climate change toward the end of the twenty-first century. *Journal of Climate*. 26:8269–8288.
- Shaw T, Baldwin M, Barnes EA, Caballero R, Garfinkel C, Hwang Y-T, Li C, O’Gorman P, Rivière G, Simpson I, et al. 2016. Storm track processes and the opposing influences of climate change. *Nature Geoscience*. 9:656–664.
- Sillmann J, Kharin VV, Zwiers FW, Zhang X, Bronaugh D. 2013. Climate extremes indices in the CMIP5 multimodel ensemble: part 2. Future climate projections. *Journal of Geophysical Research Atmospheres*. 118:2473–2493. <https://doi.org/10.1002/jgrd.50188>.
- Simpson IR, Blackburn M, Haigh JD. 2012. A mechanism for the effect of tropospheric jet structure on the annular mode-like response to stratospheric forcing. *Journal of Atmospheric Sciences*. 69:2152–2170.
- Stopa JE, Cheung KF, Tolman HL, Chawla A. 2013. Patterns and cycles in the climate forecast system reanalysis wind and wave data. *Ocean Modelling*. 70:207–220. <https://doi.org/10.1016/j.ocemod.2012.10.005>. *Ocean Surface Waves*.
- Taylor KE, Stouffer RJ, Meehl GA. 2012. An overview of CMIP5 and the experiment design. *Bulletin of the American Meteorological Society*. 93:485–498. <https://doi.org/10.1175/BAMS-D-11-00094.1>.
- Timmermans B, Stone D, Wehner M, Krishnan H. 2017. Impact of tropical cyclones on modeled extreme wind-wave climate. *Geophysical Research Letters*. 44:1393–1401.

- Tolman HL. 2009. User manual and system documentation of wavewatch III TM version 3.14. Technical note, MMAB contribution, no. 276; p. 220.
- Torsethaugen K, Faanes T, Haver S. 1984. Characteristics for extreme sea states on the Norwegian continental shelf. Technical report number NHL 2 84123. Trondheim: Norwegian Hydrodynamics Laboratories, Division River and Harbour Laboratory.
- Wandres M, Pattiaratchi C, Hemer MA. 2017. Projected changes of the southwest Australian wave climate under two atmospheric greenhouse gas concentration pathways. *Ocean Modelling*. 117:70–87. <https://doi.org/10.1016/j.ocemod.2017.08.002>.
- Wang XL, Feng Y, Swail VR. 2014. Changes in global ocean wave heights as projected using multi-model cmip5 simulations. *Geophysical Research Letters*. 41:1026–1034.
- Wang XL, Feng Y, Swail VR. 2015. Climate change signal and uncertainty in CMIP5-based projections of global ocean surface wave heights. *Journal of Geophysical Research Oceans*. 120:3859–3871.